

Selectivity in yttrium manganese oxide synthesis via local chemical potentials in hyperdimensional phase space

Paul K. Todd,^{†,#} Matthew J. McDermott,^{‡,¶,#} Christopher L. Rom,[†] Adam A. Corrao,[§] Jonathan J. Denney,[§] Shyam S. Dwaraknath,[‡] Peter G. Khalifah,^{§,||} Kristin A. Persson,^{⊥,¶} and James R. Neilson^{*,†}

[†]*Department of Chemistry, Colorado State University, Fort Collins, Colorado 80523-1872, USA*

[‡]*Materials Sciences Division, Lawrence Berkeley National Laboratory, 1 Cyclotron Road, Berkeley, CA 94720, USA*

[¶]*Department of Materials Science and Engineering, University of California, Berkeley, CA 94720, USA*

[§]*Department of Chemistry, Stony Brook University, Stony Brook, NY 11794-3400, USA*

^{||}*Department of Chemistry, Brookhaven National Laboratory, Upton, NY 11973, USA*

[⊥]*Molecular Foundry, Lawrence Berkeley National Laboratory, 1 Cyclotron Road, Berkeley, CA 94720, USA*

#These authors contributed equally to this work.

E-mail: james.neilson@colostate.edu

Abstract

In sharp contrast to molecular synthesis, materials synthesis is generally presumed to lack selectivity. The few known methods of designing selectivity in solid-state reactions have limited scope, such as topotactic reactions or strain stabilization. This contribution describes a general approach for searching large chemical spaces to identify selective reactions. This novel approach explains the ability of a nominally “innocent” Na_2CO_3 precursor to enable the metathesis synthesis of single-phase $\text{Y}_2\text{Mn}_2\text{O}_7$ – an outcome that was previously only accomplished at extreme pressures and which cannot be achieved with closely related precursors of Li_2CO_3 and K_2CO_3 under identical conditions. By calculating the required change in chemical potential across all possible reactant-product interfaces in an expanded chemical space including Y, Mn, O, alkali metals, and halogens, using thermodynamic parameters obtained from density functional theory calculations, we identify reactions that minimize the thermodynamic competition from intermediates. In this manner, only the Na-based intermediates minimize the distance in the hyperdimensional chemical potential space to $\text{Y}_2\text{Mn}_2\text{O}_7$, thus providing selective access to a phase which was previously thought to be metastable. Experimental evidence validating this mechanism for pathway-dependent selectivity is provided by intermediates identified from *in situ* synchrotron-based crystallographic analysis. This approach of calculating chemical potential distances in hyperdimensional compositional spaces provides a general method for designing selective solid-state syntheses that will be useful for gaining access to metastable phases and for identifying reaction pathways that can reduce the synthesis temperature, and cost, of technological materials.

Introduction

Molecular reactions use catalysts to increase the rate of reaction and achieve selectivity by modifying specific barriers in the reaction pathway. However, this approach cannot be readily translated to the synthesis of non-molecular compounds, which are found in a wide range of industrial applications ranging from batteries in electronic devices to cement in concrete. To achieve selective control over solid-state reactions, a necessary first step is “turning down the heat” enough to prevent non-selective phase interconversion.¹ An extreme example of this strategy is a topotactic reaction involving ion exchange in which only a single type of atom is mobile (e.g., cations² or anions^{3,4}), which has enabled lithium-ion battery technology.⁵ However, such reactions require a relatively inert framework that facilitates the mobility of these ions. Another route to selective synthesis is epitaxial strain stabilization on a single-crystal or polycrystalline substrate.⁶ While algorithms to search for suitable substrates exist,⁷ the epitaxial stabilization requires the synthesis of a chemically-compatible lattice-matched substrate, which yields only a limited amount of material that is necessarily attached to the underlying substrate.

To address the challenge of designing selective reactions in solid-state chemistry, one must have an understanding of how the reaction proceeds. Pairwise reactions at interfaces between solids dominate selection of a reaction pathway.^{8,9} With the inclusion of additional elements, as in metathesis reactions,^{10,11} one can avoid highly stable and thus unreactive intermediates, as demonstrated in the formation of MgCr_2S_4 while avoiding the inert reactant Cr_2S_3 .^{12,13} In the preparation of complex oxides, “assisted” metathesis reactions reach quantitative yields at lower temperatures than conventional ceramic reactions,¹⁴ and they can even exhibit product selectivity depending on which alkali ($A = \text{Li}, \text{Na}, \text{K}$) carbonate precursor is used. This is seen for the reactions of $3A_2\text{CO}_3 + 2Y\text{Cl}_3 + \text{Mn}_2\text{O}_3$, where in the case of Li_2CO_3 the reaction selectively forms orthorhombic YMnO_3 , Na_2CO_3 yields $\text{Y}_2\text{Mn}_2\text{O}_7$, and K_2CO_3 does not yield selectively.¹⁵

A central challenge of this contribution is to understand the origin of the different product outcomes that result from changing an ancillary precursor that is not directly involved in any elementary reaction producing a yttrium manganese oxide. In conventional stoichiometric reactions using

binary yttrium oxide and manganese oxide precursors, hexagonal YMnO_3 , denoted h- YMnO_3 , forms at temperatures greater than 950 °C.^{16,17} Previous reports have described the synthesis of $\text{Y}_2\text{Mn}_2\text{O}_7$ under high temperatures and highly oxidizing conditions (1100 °C and 4 GPa with $\text{KIO}_4 \longrightarrow \text{KIO}_3 + \frac{1}{2}\text{O}_2$)¹⁸ or hydrothermally under oxidizing conditions (NaOH , NaClO_3 in H_2O at 500 °C and 3 GPa),¹⁹ leading to its previous characterization as a metastable phase.²⁰ Interestingly, thermogravimetric analysis shows the $\text{Y}_2\text{Mn}_2\text{O}_7$ pyrochlore to be stable up to 800 °C, above which it decomposes to the perovskite YMnO_3 .¹⁹ Therefore, if $\text{Y}_2\text{Mn}_2\text{O}_7$ is stable at the lower temperatures, its stability cannot solely explain why only the sodium-based assisted metathesis precursors are selective for its formation given the low reaction temperatures for all of the alkali metathesis reactions.

Here, using temperature-dependent synchrotron powder X-ray diffraction (SPXRD) experiments to study the $\text{Y}_2\text{Mn}_2\text{O}_7$ -forming assisted metathesis reaction with a sodium precursor, $\text{Mn}_2\text{O}_3 + 2 \text{YCl}_3 + 3 \text{Na}_2\text{CO}_3 + \frac{1}{2} \text{O}_2 \longrightarrow \text{Y}_2\text{Mn}_2\text{O}_7 + 6 \text{NaCl} + 3 \text{CO}_2$, we identify a specific reaction pathway dependent on the formation of Y_2O_3 and its reaction with Na_xMnO_2 intermediates. Density functional theory (DFT) derived thermochemistry reveals that $\text{Y}_2\text{Mn}_2\text{O}_7$ is thermodynamically stable below $T \approx 1100$ °C and that sodium-based intermediates provide selective formation of this phase by circumventing the formation of other Y-Mn-O intermediates (e.g., YMnO_3 and YMn_2O_5). This sodium based reaction differs from the equivalent reactions with Li_2CO_3 and K_2CO_3 , which we previously showed instead yield YMnO_3 , with a reaction temperature as low as 500 °C.^{21,22} We attribute the selective formation of $\text{Y}_2\text{Mn}_2\text{O}_7$ to the distance of the Na-based intermediates in chemical potential space, which is shown visually on the chemical potential diagram and is numerically calculated between the stability regions of the reactants and products in a reaction. These methods, applied to easily retrievable materials data, now allow one to search for selective reactions over large, hyperdimensional compositional spaces.

Methods

Experimental methods

All reagents were prepared, stored, and weighed in an argon-filled glovebox with O₂ and H₂O levels ≤ 0.1 ppm. Manganese(III) oxide (Sigma Aldrich 99%) was purified by heating Mn₂O₃ in an alumina boat at 1 °C/min to 700 °C for 16 h in air and quenched into the glovebox; purity was verified by powder X-ray diffraction (PXRD). Manganese (IV) oxide (Sigma Aldrich $\geq 99\%$), YCl₃ (Alfa Aesar 99.9%), sodium carbonate (ACROS Organics 99.5%), and manganese (II) carbonate (Sigma Aldrich $\geq 99.99\%$) were purchased and stored under argon. All gases (O₂, Ar, He) were purchased through Airgas at the Ultra High Purity grade (99.999%). NaMnO₂ (*C2/m*) was prepared by mixing manganese (III) oxide and sodium carbonate in a 1:1 molar ratio, grinding for 15 minutes in an agate mortar and pestle, and pelleting using a 1/4 in die under ~ 1 tn of force. The pellet was placed upon a sacrificial layer of powder in an alumina crucible and heated in a muffle furnace at 1 °C/min to 700 °C for 10 h. The reaction was subsequently quenched into the antechamber of the glovebox and stored under argon. Similarly, Na_{0.7}MnO₂ (*Cmcm*) was prepared by mixing manganese (II) carbonate and sodium carbonate in a 0.70:1 Na:Mn ratio following the same pellet preparation as NaMnO₂. The reaction was performed by heating at 5 °C/min to 1050 °C for 15 h and then quenching into the antechamber of a glovebox and stored under argon. Y₂O₃ was purified of hydroxide in an alumina boat at 1 °C/min to 900 °C for 4 h in air, cooled to 200 °C at 1 °C/min for 12 h, and quenching into the glovebox. YOCl was prepared by heating YCl₃ · 6H₂O in an alumina boat to 350 °C at 10 °C/min for 4 h in air. The YOCl product formed as the *P4/nmn* PbClF structure-type. All prepared reactants were confirmed using laboratory PXRD. Preparations for *ex situ* assisted metathesis reactions have been described in detail previously where reaction yields match the expected Y₂Mn₂O₇:6NaCl by PXRD (14.2(3) mol% Y₂Mn₂O₇).¹⁵ Laboratory PXRD data were collected on a Bruker D8 Discover diffractometer using Cu K α radiation and a Lynxeye XE-T position-sensitive detector.

For temperature-dependent *in situ* assisted metathesis reactions that produce carbon dioxide as

a by-product, open-ended quartz capillaries (1.1 mm OD) were packed in a glove-bag under argon using glass wool as a plug. Synchrotron X-ray diffraction experiments were performed at beamline 17-BM-B ($\lambda = 0.2415 \text{ \AA}$) at the Advanced Photon Source (APS) at Argonne National Laboratory using a Perkin Elmer plate detector at a distance of 700 mm. All capillaries were loaded into a flow-cell apparatus equipped with resistive heating elements and heated at $10 \text{ }^\circ\text{C}/\text{min}$.²³ Gas flow (O_2 , He) was controlled through mass flow controllers at a rate of $0.2 \text{ cc}/\text{min}$. Assisted-metathesis reactions were heated to a maximum temperature of $850 \text{ }^\circ\text{C}$ while the sample continuously rocked at $\pm 5^\circ$ around the axis of the capillary. Diffraction patterns were collected every two seconds and summed every 20 seconds for powder averaging. Plate detector images were integrated using GSAS-II and calibrated using a LaB_6 standard.

All Rietveld refinements were performed using TOPAS v6. Due to the number and positional overlap of intermediates during the sequential refinements, thermal displacement parameters were fixed at 5 \AA^2 and the full-width-half-max using a Lorentzian polynomial was fixed at 178 nm to better account for changes in peak intensity during the reaction. In order to compare the relative fractions of phases determined from Rietveld calculations,²⁴ a weighted scale factor (WSF) is defined as: $Q_p = S_p \cdot V_p \cdot M_p$ where Q_p = weighted scale factor of phase p, S_p = Scale factor calculated from Rietveld for phase p, V_p is the volume of the unit cell for phase p, and M_p is the atomic mass of the unit cell for phase p. It should be noted that we omit the Brindley coefficient for microabsorption correction in our calculation of weighted scale factor due to the unreliable refinement of particle sizes for individual phases. Amorphous material and product lost as vapor are not accounted for in the sequential refinement. We reference all phases by their nominal stoichiometric formula; however, the actual chemical formula may be distinct from the written formula as XRD data alone cannot typically resolve non-stoichiometric compounds.

It has been recently demonstrated by some of us that f^* diagrams are a powerful tool for understanding defects in chemical systems with three different crystallographic sites, allowing a diffraction analog of a ternary phase diagram to be calculated in which each axis represents the relative scattering power of each crystallographic site (at $2\theta = 0$) rather than the chemical

composition.^{25,26} The f^* diagram method is applied here with a slight modification to understand the evolution of defects within the Na_xMnO_2 intermediates. The $C2/m$ P3 structure has three distinct crystallographic sites (one for each element), whereas the $Cmcm$ Birnessite P2 phase has four distinct crystallographic sites (2 Na, 1 Mn, 1 O) rather than three. Therefore, the scattering powers of the two Na sites were summed together in the construction of the f^* diagram.

Computational methods

Calculating thermodynamic free energies

DFT-based atomic structures and formation enthalpies for material phases in the Y-Mn-O-Na-Li-K chemical systems were acquired from the Materials Project (MP) database, version 20210513²⁷ Gibbs free energies of formation, $\Delta_f G^0(T)$, of solid DFT compounds were estimated using the machine-learned Gibbs free energy descriptor approach implemented by Bartel, et al.²⁸ and applied to MP data. The pymatgen package was used to perform convex hull phase stability analysis.²⁹

To model the energetics of reactions occurring in flowing O_2 gas, the grand potential energy, Φ , was used as the relevant thermodynamic potential:

$$\Phi = G(P, T) - \mu_{\text{O}} N_{\text{O}} \quad (1)$$

where Φ is normalized to the number of non-oxygen atoms. Since in place of $G(P, T)$ we used standard Gibbs free energies of formation, $\Delta_f G^0(T=650^\circ\text{C})$, the chemical potential of oxygen was assigned a value of zero, i.e., $\mu_{\text{O}} = \mu_{\text{O}}^0$ ($p = 0.1$ MPa, $T = 650$ °C). While this did not result in a shift in the total grand potential energy of any particular phase, it did change the number of atoms used for normalization and hence affected the magnitude of the normalized reaction energies, $\Delta\Phi_{\text{rxn}}$.

Construction of chemical potential diagrams

Chemical potential diagrams, as well as their more traditional two-dimensional versions (predominance diagrams), were constructed using the methodology described by Yokokawa.³⁰ We used an

algorithmic approach inspired by a similar method for construction of Pourbaix diagrams,³¹ which is briefly summarized here.

For a pure substance with N atoms per chemical formula unit, consisting of n unique elements indexed i with concentrations of x_i , its hyperplane in n -dimensional chemical space is defined via the equation:

$$\sum_{i=1}^n x_i(\mu_i - \mu_i^0) = \frac{1}{N} \Delta G_f^0(T) \quad (2)$$

where the standard Gibbs free energy of formation, $\Delta G_f^0(T)$, has been normalized to an energy-per-atom basis by dividing by the total number of atoms per formula unit, N . Note that all reference chemical potentials μ_i^0 are set to zero when working with elements in their standard states.

Following the construction of hyperplanes for all phases in the chemical system, the stability domains are acquired by taking the convex hull of all points belonging to that phase in the set of intersections of the lowest energy hyperplanes, as calculated with the `HalfspaceIntersection` code implemented in SciPy.³² In this construction, each stability region is a convex $n - 1$ dimensional polytope in n -dimensional chemical potential space. Since many possible chemical reactions involve more than $n = 3$ elements, we must take additional steps to visualize the hyperdimensional ($n > 3$) phase boundaries relevant to the reactions in this work. This can be accomplished by 1) using clever transformations of the axes, 2) setting one or more chemical potentials to fixed values, or 3) taking a slice of the relevant chemical potential polytopes in lower dimensions. Here we choose the third option, which uniquely allows for comparison across the full Y-Mn-O-Na-Li-K-Cl assisted metathesis system. Phases that do not directly appear on the generalized chemical potential diagram in three dimensions, e.g., AMnO_2 in the Y-Mn-O subspace, are thus computed first in higher dimension chemical potential space (A-Y-Mn-O) and then sliced to plot in lower-dimensional subspace. In the case of AMnO_2 , these regions appear as three-dimensional polyhedra due to the added degree of freedom in the chemical potential of the alkali element, μ_A . These polyhedra also at least partially contact the stability areas of Y-Mn-O compounds, indicating where phases are adjacent in higher-dimensional space.

The “chemical potential distance”, $\Delta\mu_{\min}(P_a, P_b)$, between any two phases P_a and P_b was calculated geometrically by finding the minimum Euclidean distance between the domains (i.e., the convex stability polytopes) of each phase on the chemical potential diagram. This was accomplished practically by computing the minimum Euclidean distance between all pairs of vertices (μ_{a_i}, μ_{b_j}) defining each of the two convex polytopes of phases P_a and P_b :

$$\Delta\mu_{\min}(P_a, P_b) = \min_{i,j} \{ \|\mu_{a_i} - \mu_{b_j}\| \} \quad (3)$$

While the minimum distance between vertices is not necessarily equivalent to the minimum distance between any facet of the polytopes, the implementation of the more accurate distance calculation is nontrivial. We thus found the vertex based k-d tree method, as implemented in SciPy, to be an appropriate trade-off between computational complexity and accuracy.

Enumerating reactions with $\text{Y}_2\text{Mn}_2\text{O}_7$ as a product

Chemical reactions with $\text{Y}_2\text{Mn}_2\text{O}_7$ as a product were enumerated via a network-based approach described in a previous work³³ and implemented in the reaction-network Python package.³⁴ To summarize, the enumeration approach is a combinatorial brute force approach whereby every combination of phases up to a size of n is considered both as a possible set of reactants or products. The set of all possible reactions is calculated by taking the Cartesian product between the set of reactant phase combinations and product phase combinations and filtering by whether it is possible to write a stoichiometrically balanced reaction equation between the reactants and products. In this work, reactions up to a size $n = 2$ are enumerated from the set of 2,878 phases predicted to be stable at $T = 650^\circ\text{C}$ within the alkali metal (Li, Na, K, Rb, Cs), halogen (F, Cl, Br, I), carbon (C), and target (Y, Mn, O) chemical system. To account for the system being open to oxygen gas, we also consider reaction equations with oxygen as an optional reactant or product beyond the $n = 2$ limitation.

The enumerated reactions were compared against each other by using both the normalized reaction free energy and a “total” chemical potential distance for the reaction as “cost” variables.

For the purposes of ranking reactions, the total cost of a reaction, C , was calculated using the softplus function with an equally weighted mean between the two cost variables:

$$C = \ln \left(1 + \frac{273}{T} \exp \left(\frac{\Delta\Phi_{\text{rxn}} + \sum \Delta\mu_{\text{min}}}{2} \right) \right) \quad (4)$$

where T corresponds to a temperature of $T = 923$ K, the reaction energy, $\Delta\Phi_{\text{rxn}}$, corresponds to the normalized change in grand potential energy, and $\sum \Delta\mu_{\text{min}}$ represents the total chemical potential distance for a reaction, which is calculated as the sum of the (minimum) chemical potential distances between all possible pairwise interfaces in the reaction, excluding the interface(s) between the reactants. For example, in the hypothetical reaction $A+B \rightarrow C+D$, the total chemical potential distance is calculated by taking the summation of $\Delta\mu_{\text{min}}(A, C)$, $\Delta\mu_{\text{min}}(A, D)$, $\Delta\mu_{\text{min}}(B, C)$, $\Delta\mu_{\text{min}}(B, D)$, and $\Delta\mu_{\text{min}}(C, D)$.

The full set of enumerated chemical reactions, as well as all experimental raw data, processed data, data processing scripts, and figure plotting scripts, are available at <https://github.com/GENESIS-EFRC/y2mn2o7-selectivity>. The entire reaction enumeration and ranking approach has also been implemented within the aforementioned reaction-network Python package³⁴ and can be applied in a similar fashion to recommend precursors for synthesizing other target materials. The applicability of this approach beyond the Y-Mn-O system is the subject of future work(s).

Results and Discussion

Reaction pathway from phase evolution

In situ synchrotron powder X-ray diffraction (SPXRD) studies were used to identify the intermediate phases and reaction pathways that permit the selective formation of $\text{Y}_2\text{Mn}_2\text{O}_7$ through assisted metathesis reactions with Na_2CO_3 . Figure 1 shows the integrated SPXRD diffraction patterns collected during a reaction using precursor phases of $\text{Mn}_2\text{O}_3 + 2\text{YCl}_3 + 3\text{Na}_2\text{CO}_3$. Data were collected during heating to 650°C at $10^\circ\text{C}/\text{min}$ then dwelling at 650°C for 60 min, performed under

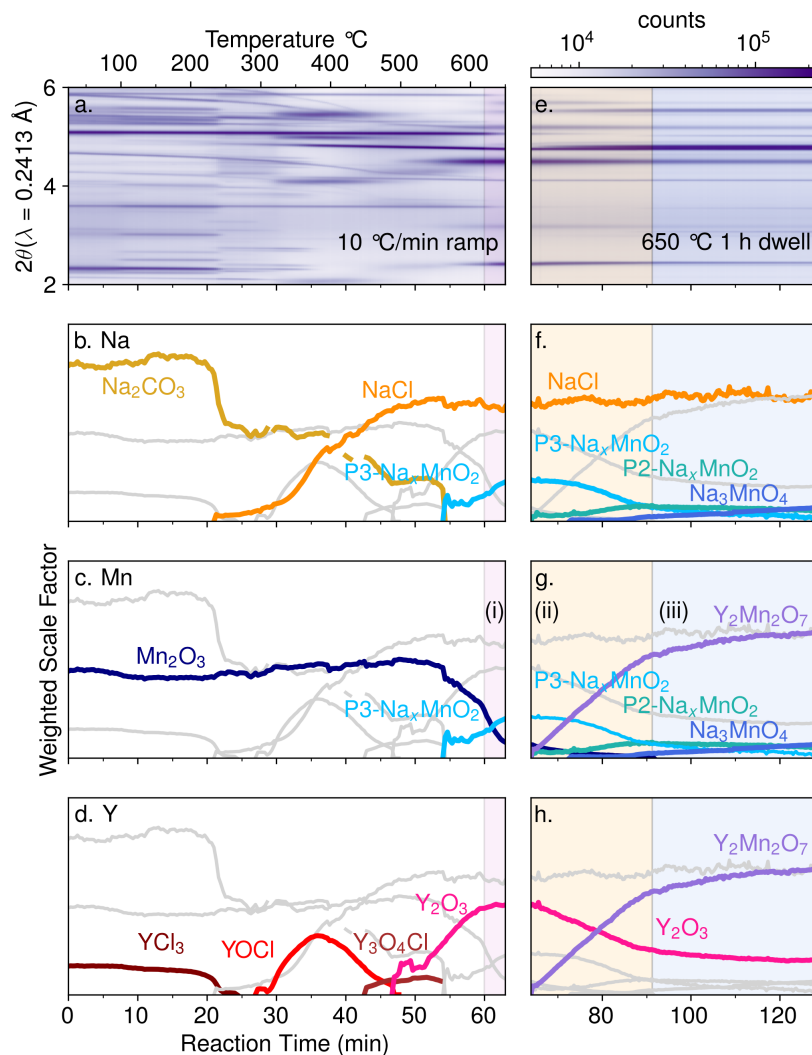


Figure 1: *In situ* SPXRD data and calculated weighted scale factors from sequential Rietveld analysis as a function of time for the reaction: $\text{Mn}_2\text{O}_3 + 2 \text{YCl}_3 + 3 \text{Na}_2\text{CO}_3 + \frac{1}{2} \text{O}_2 \longrightarrow \text{Y}_2\text{Mn}_2\text{O}_7 + 6 \text{NaCl} + 3 \text{CO}_2$ under flowing oxygen. The reaction is separated into two main vertical panels: (a-d) heating at 10 °C/min to 650°C and (e-h) dwelling at 650 °C for 60 min. **a,e**, The *in situ* diffraction data plotted using a false color representation of the diffraction counts. Calculated weighted scale factors of phases over the course of the reaction are plotted and separated into horizontal panels by cation element: **b,f**, sodium, **c,g**, manganese, and **d,h**, yttrium. The gray lines in each horizontal panel show the observed phases containing the other cations. The shaded regions, (i), (ii), and (iii), correspond to trajectories highlighted in Figure 5.

flowing oxygen. Quantitative phase analysis using the Rietveld method reveals the identities and phase fractions of intermediates of $P3\text{-Na}_x\text{MnO}_2$, $P2'\text{-Na}_x\text{MnO}_2$, YOCl , $\text{Y}_3\text{O}_4\text{Cl}$, Y_2O_3 ; products of NaCl and $\text{Y}_2\text{Mn}_2\text{O}_7$; and a small amount of Na_3MnO_4 impurity, as summarized in Figure 1. No other yttrium manganese oxide phases were observed.

The relevant intermediates that exist at the onset of formation of $\text{Y}_2\text{Mn}_2\text{O}_7$ are Y_2O_3 , $P3\text{-Na}_x\text{MnO}_2$, and a small amount of Mn_2O_3 . Y_2O_3 forms with a very small particle size (less than ~ 35 nm, Figure S2), and its production yields a large fraction of the expected NaCl product (Figure 1). $P3\text{-Na}_x\text{MnO}_2$ forms directly from the reaction of Na_2CO_3 and Mn_2O_3 , in agreement with a previous *in situ* and computational study.⁹ Once both of these key intermediates are present, $P3\text{-Na}_x\text{MnO}_2$ then reacts with Y_2O_3 to form pyrochlore $\text{Y}_2\text{Mn}_2\text{O}_7$, also triggering the formation of $P2'\text{-Na}_x\text{MnO}_2$ (*Cmcm* structure, with a slight shear of the ideal $P2\text{-}P6_3/mmc$ structure).^{35–37} Thereafter, selective formation of $\text{Y}_2\text{Mn}_2\text{O}_7$ is sustained through the reaction of $P2'\text{-Na}_x\text{MnO}_2$ with Y_2O_3 . After $P3\text{-Na}_x\text{MnO}_2$ is fully consumed, the rate of $\text{Y}_2\text{Mn}_2\text{O}_7$ production slows dramatically, as Na_3MnO_4 gradually forms (Fig 1). Na_3MnO_4 does not appear in reaction products of *ex situ* studies of these assisted metathesis reactions performed on bulk scales, although it may be present as a trace quantity.¹⁵

Thermodynamic stability of $\text{Y}_2\text{Mn}_2\text{O}_7$

Evaluation of the Y-Mn-O phase diagram reveals that $\text{Y}_2\text{Mn}_2\text{O}_7$ is thermodynamically stable (i.e., it is on the convex hull) at low temperatures ($T \leq 1100$ °C). Using error-corrected formation energies derived from DFT calculations³⁸ and a previous Gibbs free energy model for solids,²⁸ the phase diagram of the Y-Mn-O system has been calculated at finite temperatures relevant to the synthesis reactions being investigated, with results of calculations at 650 °C and 1200 °C shown in Figure 2. Figure 2a depicts that the predominance area of $\text{Y}_2\text{Mn}_2\text{O}_7$ is quite small, indicating its low relative stability with respect to thermodynamic decomposition to neighboring phases. For a 1:1 Y:Mn composition ratio in an environment open to oxygen, h-YMnO_3 is thermodynamically stable at all temperatures and under a wide range of oxygen chemical potentials, while $\text{Y}_2\text{Mn}_2\text{O}_7$

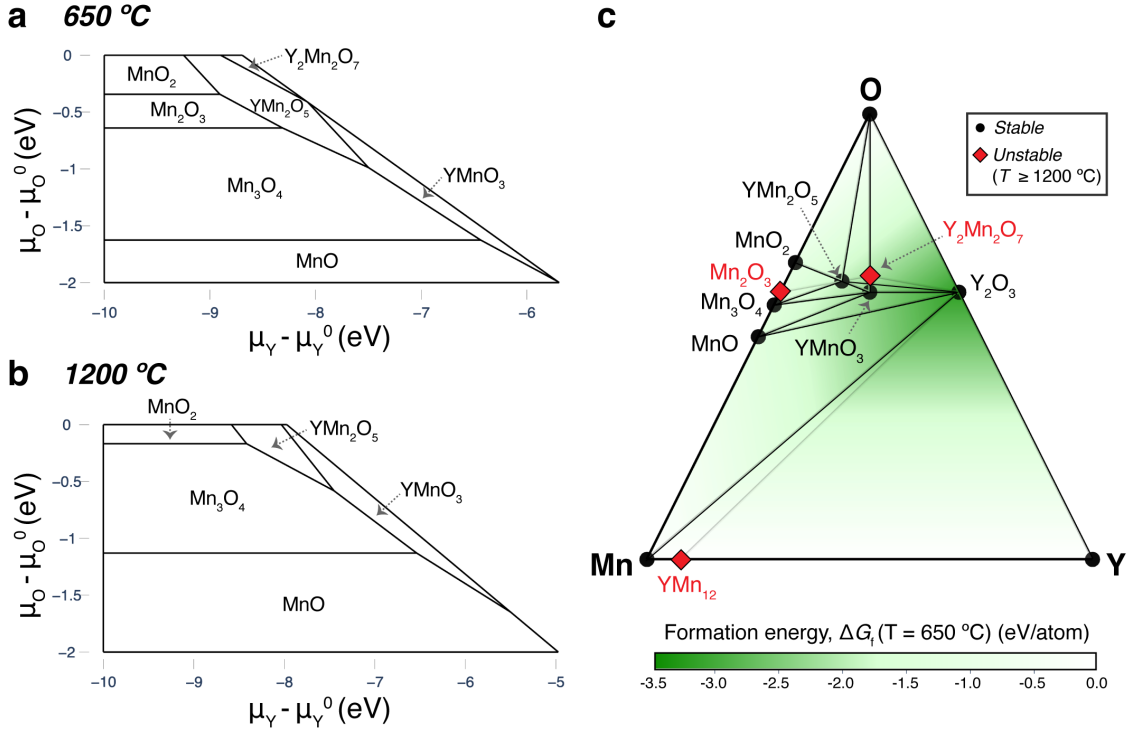


Figure 2: Computed phase stabilities in the Y-Mn-O chemical system. Predominance diagrams are shown as a function of oxygen and yttrium chemical potentials, μ_O and μ_Y , at temperatures of **a**, 650 °C and **b**, 1200 °C, referenced to their standard elemental state. **c**, Predicted ternary compositional phase diagram for the Y-Mn-O system at 1200 °C (black lines/circles) overlaid on the phase diagram at 650 °C, where red squares and gray lines mark phases and facets that are destabilized at $T \geq 1200$ °C, respectively. $Y_2Mn_2O_7$ is predicted to be stable at low temperatures ($T \leq 1100$ °C). Gibbs free energies of formation are estimated by applying a machine-learned transformation²⁸ on DFT-based formation enthalpies acquired from the Materials Project database.²⁷

is thermodynamically stable only below ~ 1100 °C and at higher oxygen chemical potentials (i.e., oxygen rich conditions). While the predicted temperature below which $Y_2Mn_2O_7$ is stable is overestimated by these calculations since only h- $YMnO_3$ was observed to form at 950 °C in experiments,¹⁷ the low-temperature thermodynamic stability of $Y_2Mn_2O_7$ is assessed experimentally here by heating $Y_2Mn_2O_7$ in flowing oxygen at 650 °C for two weeks (Figure S12), a result that is in agreement with previous thermogravimetric analysis.¹⁹ The fact that the Li_2CO_3 and K_2CO_3 precursors do not produce the thermodynamically favored phase of $Y_2Mn_2O_7$ at temperatures below 950 °C and $p(O_2) = 1$ atm (i.e., $\mu_O - \mu_O^0 \approx 0$) indicates that the metathesis reaction temperatures

are sufficiently low to yield kinetic control in the formation of o-YMnO₃ or h-YMnO₃.³⁹ Finally, it indicates the need for a deeper understanding of the specific factors that determine which reaction pathway is followed for a given alkali carbonate precursor.

Product selectivity via chemical potential distances

We hypothesize that the generalized chemical potential diagram, which was previously devised as a three-dimensional extension of predominance diagrams with application to modeling interface stability and reactivity,³⁰ clarifies the large differences in product selectivity that arise by changing the identity of the alkali precursor. As the mathematical dual to the convex hull of the extensive energy-composition space, the generalized chemical potential diagram explicitly defines phase stability regions as bounded convex $n - 1$ dimensional polytopes within the full n -dimensional, intensive chemical potential space. Although in principle the chemical potential diagram conveys identical information as the traditional compositional phase diagram, it has the unique advantage of directly revealing the *relative* stability of phases. In fact, the volume of each phase's stability polytope increases with its energy "below" the convex hull, i.e., the energy that would be released forming this phase via decomposition from the neighboring phases within a facet of the hull. The chemical potential diagram also directly links thermodynamic phase construction with atomic diffusion, and its construction even permits the visualization of diffusion paths in solid-state reactions.³⁰ Hence the chemical potential diagram is well-suited for application to understanding and predicting the local behavior of reactions at solid interfaces.

Selective reactions in solid state chemistry need to minimize the probability of forming an undesired product phase at any point in time during the reaction pathway. As has been previously proposed,⁴⁰ a reaction at the interface between two solid phases can proceed through either interface control or diffusion control, the latter resulting in local thermodynamic equilibrium and the corresponding requirement that elemental chemical potentials be continuous across the interfaces between reactants and product phase(s). All solid-state reactions eventually tend towards diffusion control as the product layer thickness grows. For this reason, predicted reactions which

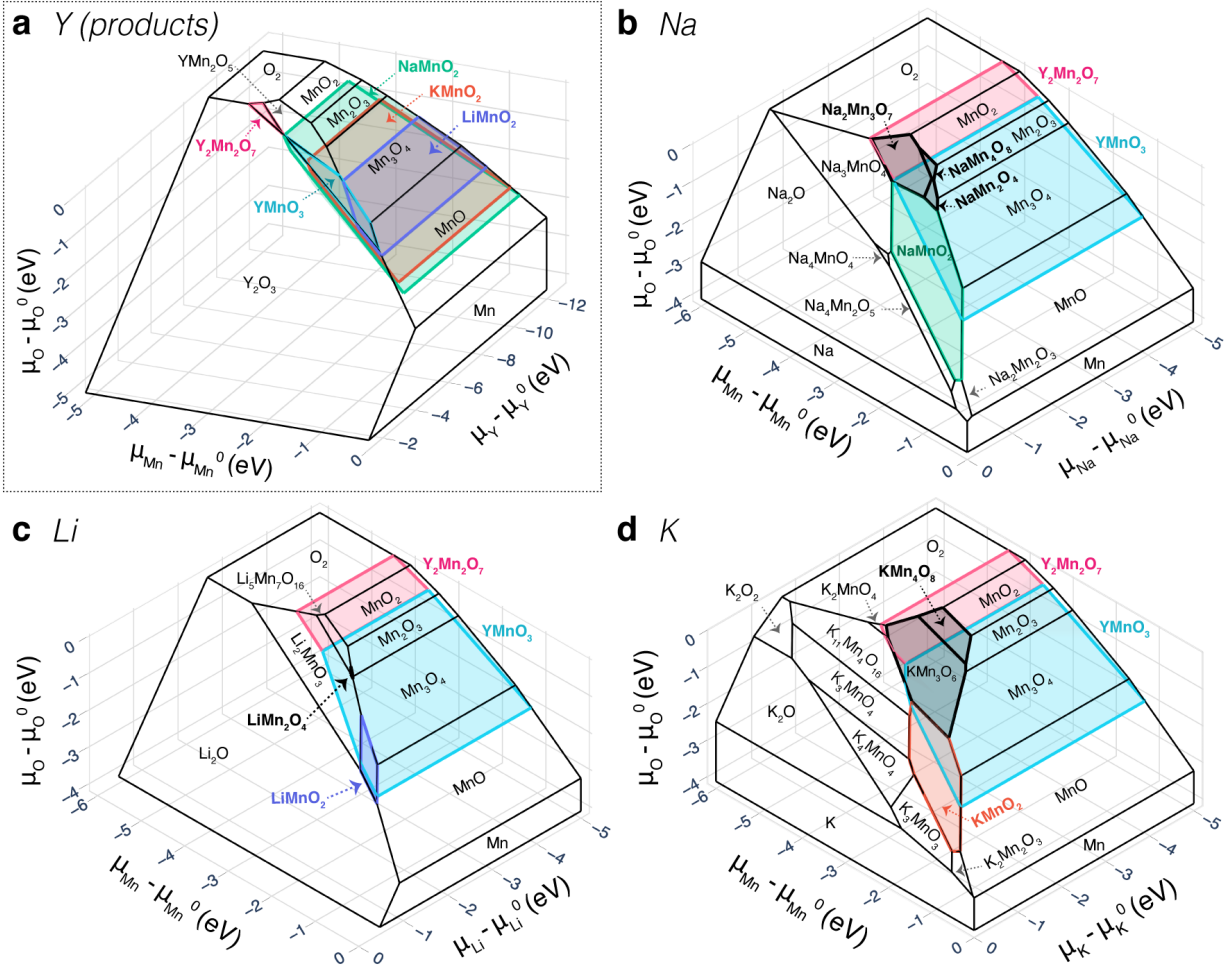


Figure 3: Chemical potential diagrams of the Y-Mn-O-Na-Li-K system at 650 °C, plotted in product (boxed) and reactant subspaces. **a**, Y-Mn-O product subspace where the stability polytopes of stoichiometric NaMnO_2 (green), LiMnO_2 (purple), and KMnO_2 (orange) have been plotted as lower-dimensional slices, appearing as thin polyhedra due to the added degree of freedom (μ_Y). The NaMnO_2 polyhedron extends to high enough μ_O and low enough μ_{Mn} to reach $\text{Y}_2\text{Mn}_2\text{O}_7$, while the LiMnO_2 and KMnO_2 polyhedra do not. As such, LiMnO_2 and KMnO_2 suggest the formation of YMnO_3 and/or YMn_2O_5 depending on the value of μ_Y , as previously observed.^{15,21,22} **b-d**, A-Mn-O reactant subspaces with visualized slices of the YMnO_3 (cyan) and $\text{Y}_2\text{Mn}_2\text{O}_7$ (magenta) polytopes. The other shaded areas (gray) highlight A_xMnO_2 intermediates (and structurally-related neighbors) that lead directly to the formation of yttrium manganese oxide products.

pose synthetic challenges are those in which it is impossible to achieve local equilibrium without decomposition to other phases before formation of the equilibrium product. On the chemical potential diagram, such reactions involve reactant-product pairs which do not share a phase boundary.

Considering the reaction $\text{Y}_2\text{O}_3 + \text{Mn}_2\text{O}_3 \longrightarrow 2 \text{YMnO}_3$, if local equilibrium is achieved during the reaction, then according to Figure 3a, one expects YMn_2O_5 and/or Mn_3O_4 to form before formation of the final YMnO_3 product, consistent with the results of control reactions presented in Figure S10 and the previously-reported phase diagram.¹⁷

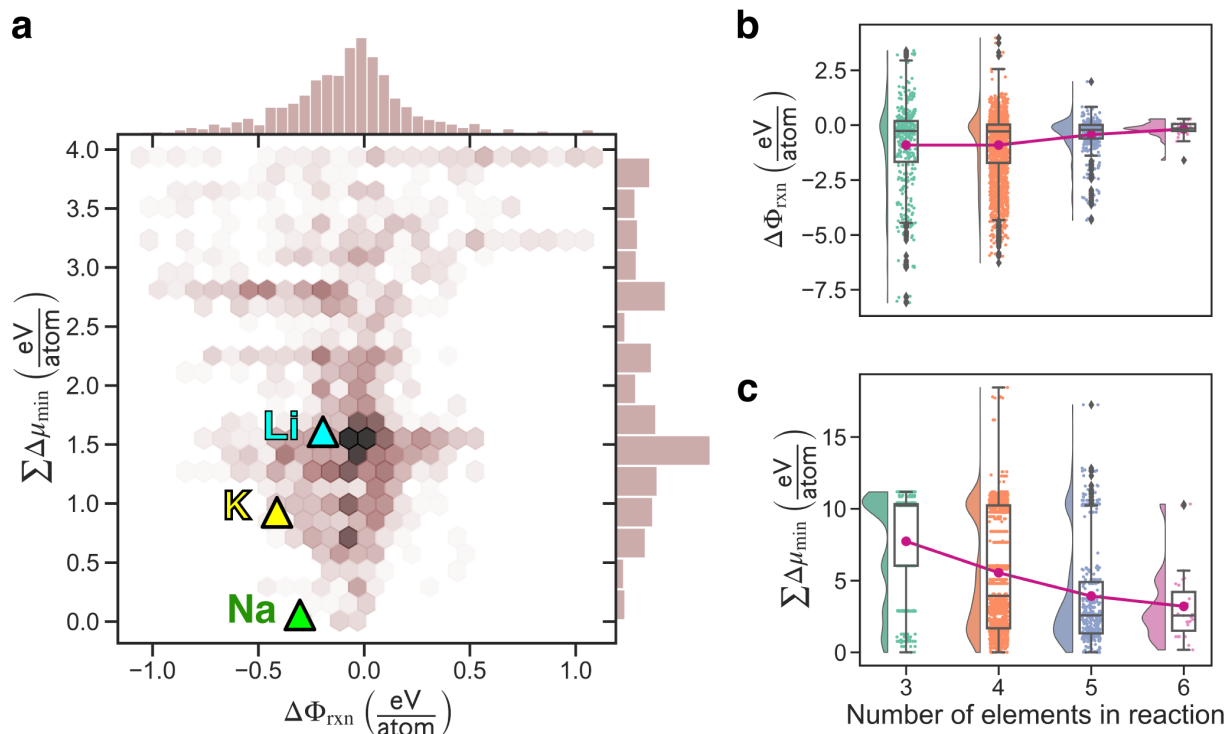


Figure 4: Energy and total chemical potential distance distributions for 3,017 predicted chemical reactions forming $\text{Y}_2\text{Mn}_2\text{O}_7$. The reactions were predicted from a chemical space consisting of all alkali metals (Li, Na, K, Rb, Cs), halogens (F, Cl, Br, I), carbon (C), and the target elements (Y, Mn, O). Oxygen was treated as an open element with a chemical potential corresponding to μ_{O}^0 ($p = 0.1 \text{ MPa}$, $T = 650 \text{ }^\circ\text{C}$). **a**, A hexbin plot showing the distribution of reaction energies (in grand potential), $\Delta\Phi_{\text{rxn}}$, and calculated total chemical potential distance values, $\Sigma\Delta\mu_{\text{min}}$ for each reaction. The three colored triangles indicate the specific reactions $2 \text{AMnO}_2 + 2 \text{YOCl} + \frac{1}{2} \text{O}_2 \longrightarrow \text{Y}_2\text{Mn}_2\text{O}_7 + 2 \text{ACl}$ for $A=\text{Li, Na, K}$. **b,c**, Distributions of reaction energies and total chemical potential distances as a function of the number of elements in the reaction. All reactions include at least the three elements of the target phase (Y, Mn, O). The mean values for each distribution are connected by a magenta line.

Therefore, selective reactions are those which can be balanced, produce the desired product, and minimize the distance in chemical potential space between pairwise reactant-product interfaces. On the chemical potential diagram, this manifests as determining whether each reactant-

product pair shares a boundary (i.e., zero distance) or is separated by the polytope(s) of one or more additional phases (i.e., non-zero distance). This also applies to product-product pairs, which may further react if they do not share a boundary on the chemical potential diagram. Plotting trial reactants in the three-dimensional chemical potential subspace of the product (Figure 3a), or plotting products in the reactant subspace (Figure 3b-d), permits direct visualization of the pairwise interfaces that control reactivity.^{8,9} This “chemical potential distance”, $\Delta\mu_{\min}$ is geometrically calculated for all reactant-product and product-product interfaces in a reaction by determining the minimum Euclidean distance between polytopes (see Methods). The primary advantage of calculating a distance value rather than a Boolean variable for whether or not two phases share a boundary is that the distance is more robust against inaccuracies in thermochemical data and conveys the degree to which the competing phases may interfere with the selectivity of the reaction.

Visualizing three-dimensional slices of the full Y-Mn-O-Na-Li-K chemical potential space reveals why only the sodium-based intermediates lead to formation of $\text{Y}_2\text{Mn}_2\text{O}_7$. Figure 3a illustrates slices of the stoichiometric AMnO_2 intermediates in the Y-Mn-O product chemical potential space. The NaMnO_2 stability polyhedron extends well beyond the range of both the LiMnO_2 and KMnO_2 phases. In fact, this Na-containing phase extends into high enough μ_{O} values to reach the stability area for $\text{Y}_2\text{Mn}_2\text{O}_7$. This enhanced stability of the NaMnO_2 phase into higher oxygen (and lower manganese) chemical potentials suggests that it may be uniquely capable of forming a stable interface with $\text{Y}_2\text{Mn}_2\text{O}_7$ and facilitating direct reaction to this pyrochlore phase. Specifically, the nearly shared boundary between the NaMnO_2 intermediate and $\text{Y}_2\text{Mn}_2\text{O}_7$ means that the reaction kinetics should be facile since the local chemical potentials of Mn and O do not need to change as the intermediate converts to the product. Furthermore, even though the *global* oxygen chemical potential is controlled through partial pressure of O_2 , the reaction of NaMnO_2 provides *locally* available oxygen at the chemical potential required to form $\text{Y}_2\text{Mn}_2\text{O}_7$. In the case of the A = Li, K precursors, the lack of available oxygen with an appropriately high chemical potential necessitates the reaction to proceed through other intermediates before it is even possible to reach $\text{Y}_2\text{Mn}_2\text{O}_7$.

The complementary inverse slices of the Y-Mn-O ternaries within the reactant A-Mn-O spaces

(Figure 3b-d), along with the study of the atomic structures of the AMnO_2 phases, provide further explanation as to why the sodium-based intermediates facilitate reaction to $\text{Y}_2\text{Mn}_2\text{O}_7$ even for Na-deficient phases, Na_xMnO_2 (where $x < 1$). In agreement with prior work,⁴¹ the sodium-based phases show a strong preference for the layered $\alpha\text{-NaFeO}_2$ -type structures relative to tunnel-like (e.g., Ramsdellite-derived) or spinel-derived structures. $\text{Na}_2\text{Mn}_3\text{O}_7$, NaMn_2O_4 , and NaMn_4O_8 , illustrated as gray shaded areas in Figure 3b, are all predicted to share the structurally analogous layered framework with stoichiometric NaMnO_2 (Figure S15a). Together these structures create an interconnected pathway along the Na-Mn-O chemical potential surface towards higher oxygen chemical potentials where the surface touches the $\text{Y}_2\text{Mn}_2\text{O}_7$ product (e.g., oxidation states ranging from +3 to +5 depending on the nature of the vacancies and whether the composition is Na-poor or Mn-poor). In contrast, LiMnO_2 has a narrower range of stability than its neighboring Li-Mn-O phases, which each prefer distinct non-layered structures (Figure S15b). In both the Li_2CO_3 assisted metathesis reactions²¹ and the direct reaction between LiMnO_2 and YOCl ,²² we observed formation of YMnO_3 and YMn_2O_5 , suggesting that the decreased range of chemical potentials over which layered LiMnO_2 is stable and lack of structural homology between the Li_xMnO_2 phases inhibits the accessibility of $\text{Y}_2\text{Mn}_2\text{O}_7$ (e.g., due to rearrangement of the phases into spinel-derived structures). Finally, in the K_2CO_3 assisted metathesis reactions, no product selectivity was observed as the reaction produced a mixture of YMnO_3 , YMn_2O_5 , and $\text{Y}_2\text{Mn}_2\text{O}_7$ products.²¹ While the K_xMnO_2 phases indeed exhibit a similar extension into high oxygen chemical potentials akin to Na_xMnO_2 (Figure 3d), the stoichiometric KMnO_2 ground-state structure does not follow the layered (nor even another another common) MnO_2 framework,⁴¹ (Figure S15c) although the layered phase is predicted to be about 44 meV/atom higher in energy than the ground state. We thus conclude that similar to Li, the K-based system lacks the structural connectivity for interconversion between different K_xMnO_2 intermediates, although direct formation of K-deficient phases may promote formation of $\text{Y}_2\text{Mn}_2\text{O}_7$. In both the Li and K systems, the initial formation of YMnO_3 or YMn_2O_5 hence imposes significant kinetic barriers to the formation of $\text{Y}_2\text{Mn}_2\text{O}_7$. According to the chemical potential diagrams, YMnO_3 would have to decompose into YMn_2O_5 and Y_2O_3 en

route to forming $\text{Y}_2\text{Mn}_2\text{O}_7$, which is consistent with myriad control experiments between binary yttrium and manganese oxides, with or without the presence of sodium (see Figures S10 and S11). Based on these observations, we argue that the minimized chemical potential distance presented in Figures 3 and 4 and ability of sodium-based intermediate to interconvert across a wide range of stoichiometries and oxidation states explain why sodium provides selectivity of $\text{Y}_2\text{Mn}_2\text{O}_7$ via a kinetically-viable pathway at lower temperatures.

Analysis of 3,017 unique chemical reactions predicted to form $\text{Y}_2\text{Mn}_2\text{O}_7$ within the full alkali metal (Li, Na, K, Rb, Cs), halogen (F, Cl, Br, I), carbon (C), and target (Y, Mn, O) chemical system show that the Na-based ternary metathesis reaction, $2 \text{NaMnO}_2 + 2 \text{YOCl} + \frac{1}{2} \text{O}_2 \longrightarrow \text{Y}_2\text{Mn}_2\text{O}_7 + 2 \text{NaCl}$ is the most optimal reaction for both minimizing the total chemical potential distance and maximizing the (negative) grand potential energy of reaction, $\Delta\Phi_{\text{rxn}}$, when these two parameters are weighted equally (see Methods). This result suggests that the Na-based pathway is not only a good pathway for producing $\text{Y}_2\text{Mn}_2\text{O}_7$ but that it may also be the most suitable metathesis reaction for making this product. The full set of reactions and their weighted rankings can be found in provided data in the Supporting Information. The energy and total chemical potential distributions for these reactions illustrate that the Na-based reaction (green triangle in Figure 4a) optimizes both total chemical potential distance and overall reaction energy. The Na-based reaction has a near-zero total chemical potential distance (0.055 eV/atom) that is significantly smaller than those of the Li and K reactions (1.608 and 0.924 eV/atom respectively) and has a more negative reaction energy than any other reaction pathway with a near-zero total chemical potential distance. Figure 4 also reveals a major design principle behind using an expanded chemical space with metathesis reactions – the addition of other elements beyond those of the target phase (Y, Mn, O) can decrease the mean total chemical potential distance of the reaction without significantly changing the mean reaction energy. This hence provides many more opportunities for finding selective reactions beyond those that exclusively contain the target chemical species, i.e., 3,017 reactions in the full 13-element chemical system vs. 362 potential reactions in the Y-Mn-O chemical system.

Direct ternary metathesis reactions carried out between Na_xMnO_2 and YOCl do indeed form $\text{Y}_2\text{Mn}_2\text{O}_7$ as predicted, but they also reveal important mechanistic details missing from the presented thermodynamic analysis that impacts product selectivity. For example, available density functional theory data is highly focused on stoichiometric compounds but tends to be lacking for solid solution and defect-containing phases. The reaction $\text{NaMnO}_2 + \text{YOCl} \xrightarrow{\text{O}_2}$ results in some $\text{Y}_2\text{Mn}_2\text{O}_7$ formation, but also the formation of YMnO_3 and YMn_2O_5 (Figure S13), suggesting that the evolution of the Na_xMnO_2 precursor during the reaction is important to consider, as illustrated in Figure 3b. A partially-oxidized precursor in the reaction, $\text{P2}'\text{-Na}_{0.7}\text{MnO}_2 + \text{YOCl}$ selectively yields $\text{Y}_2\text{Mn}_2\text{O}_7$, but the reaction is incomplete after 24 h (Figure S14). Together, these control reactions suggest that the reaction rates also depend on the specific nature of defects present in the reactants and intermediates.

Mechanistic facilitation through defect reactions

As the reaction pathway of the Li-based assisted metathesis reaction was previously reported,²¹ we focus on how Na_xMnO_2 -based intermediates react in a manner consistent with the predicted thermodynamic connectivity. Crystallographic analysis of the Na_xMnO_2 phases by free refinement of the crystallographic site occupancies of all elements in each Na_xMnO_2 structure and their subsequent analysis on an f^* diagram²⁵ together reveal how the stoichiometry of Na_xMnO_2 changes through three different defect reactions along the reaction pathway for $\text{P3-Na}_x\text{MnO}_2$ (Figure 5) and for $\text{P2}'\text{-Na}_x\text{MnO}_2$ (Figure S7). While the exact compositions defined by the site occupancies are correlated with other refinement variables (e.g., atomic displacement parameters, as addressed in the Supporting Information), the compositional trajectories observed in Figure 5 are robust.²⁵ Two distinct compositional trajectories of the $\text{P3-Na}_x\text{MnO}_2$ phase on Figure 5 follow two major processes during the reaction pathway: (i) $\text{P3-Na}_x\text{MnO}_2$ formation and (ii) reaction of $\text{P3-Na}_x\text{MnO}_2$ to yield $\text{Y}_2\text{Mn}_2\text{O}_7$ and $\text{P2}'\text{-Na}_x\text{MnO}_2$. Additionally, delineation of trajectory (iii) describes when $\text{P2}'\text{-Na}_x\text{MnO}_2$ begins reacting to yield $\text{Y}_2\text{Mn}_2\text{O}_7$.

The reaction of the $\text{P3-Na}_x\text{MnO}_2$ follows a compositional trend in chemical potential space

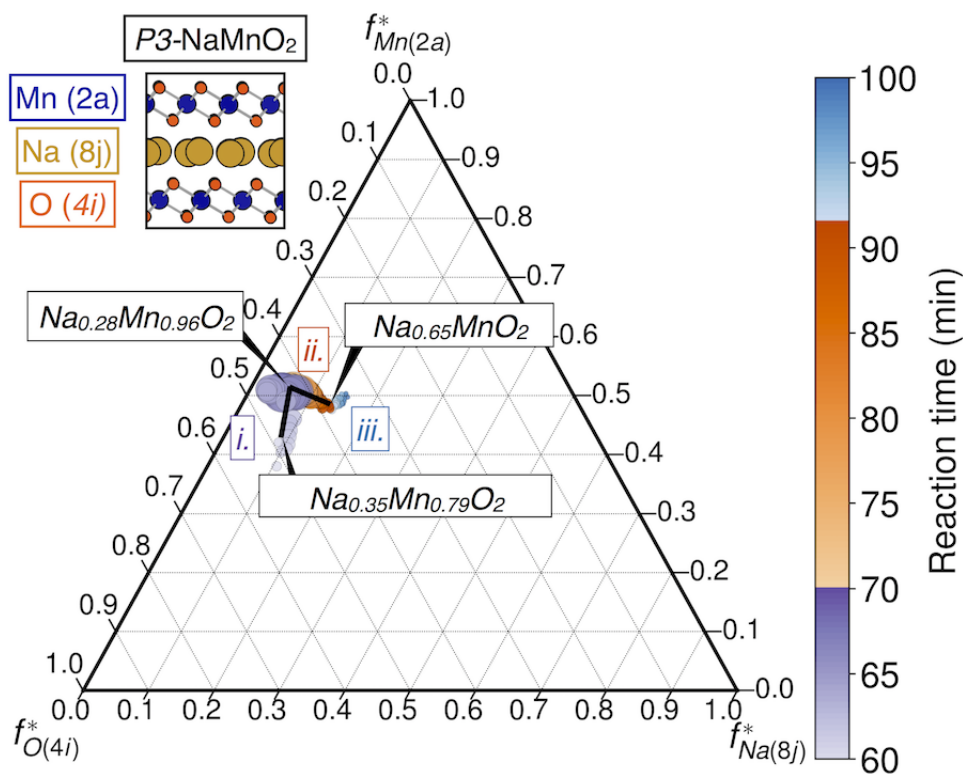


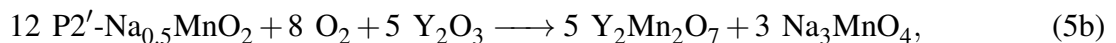
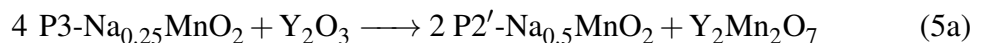
Figure 5: Compositional variation of the $P3\text{-Na}_x\text{MnO}_2$ intermediate determined by Rietveld analysis. In the f^* diagram, each axis denotes the X-ray scattering power from a crystallographic Wyckoff site within the lattice. For reference, calculated trajectories that correspond to the different stoichiometries of $P3\text{-Na}_x\text{MnO}_2$ are provided as black lines. The color bar in the figure follows the evolution of the $P3\text{-Na}_x\text{MnO}_2$ intermediate in the assisted metathesis reaction presented in Figure 1 with highlighted trajectories (i-iii) reflecting shaded regions in Figure 1(i-iii). The diameter of each circle mirrors the calculated weighted scale factor (WSF) in Figure 1 for $P3\text{-Na}_x\text{MnO}_2$ and thus corresponds to the amount of this layered phase. The structure of $P3\text{-Na}_x\text{MnO}_2$ is shown with Wyckoff atom sites labeled. The figure contains compositions for which the WSF is greater than 20% of the maximum WSF for the phase shown in Figure 1. Detailed analysis of individual site occupancies is provided in the SI.

towards the $\text{Y}_2\text{Mn}_2\text{O}_7$ product (Figure 3). The initial formation of $P3\text{-Na}_x\text{MnO}_2$ results in a very sodium-deficient composition, $P3\text{-Na}_{0.29}\text{Mn}_{0.96}\text{O}_2$. This manifests crystallographically as an excess of scattering intensity on the sodium site relative to the manganese site, suggestive of anti-site disorder, as well as decreased scattering relative to oxygen, suggestive of metal deficiency (Figure 5, as described in detail in the Supporting Information), which is also observed in the initial formation of LiNiO_2 .⁴² Additionally, there is decreased scattering intensity of the metal sites relative to oxygen, which suggests the existence of overall cation deficiencies in the structure, cal-

culated as $\text{Na}_{0.35}\text{Mn}_{0.79}\text{O}_2$ from Rietveld analysis of the PXRD data. The composition evolves in time through a cation-ordering reaction, where manganese occupying the (8j) sodium site moves to the manganese (2a) site (trajectory (i) in Figure 5). Movement along trajectory (i) yields site ordering as the phase fraction is increased; the proposed stoichiometry is analytically calculated as the black line overlaid on these data in Figure 5 (see Eqn. 3). This ordering reaction yields a calculated composition of $\text{P3-Na}_{0.29}\text{Mn}_{0.96}\text{O}_2$ at its maximal phase fraction observed in Figure 1. At that point in the overall reaction, this intermediate with a relatively high oxygen chemical potential (Figure 3b) reacts to form $\text{Y}_2\text{Mn}_2\text{O}_7$.

There is a change in the defect chemistry of $\text{P3-Na}_x\text{MnO}_2$ consistent with the loss of $\text{Mn}^{4+} + 2\text{O}^{2-}$, concomitant with consumption of Y_2O_3 and production of $\text{Y}_2\text{Mn}_2\text{O}_7$ and $\text{P2}'\text{-Na}_x\text{MnO}_2$. Along trajectory (ii) in Figure 5, there is a decrease in relative electron density from the oxygen site (4i), as well as an increase in the sodium to manganese site ratio, as described by Eqn. 4. This reflects a change in defect chemistry along trajectory (ii) from the $\text{P3-Na}_{0.29}\text{Mn}_{0.96}\text{O}_2$ calculated composition at the end of trajectory (i) to that of $\text{P3-Na}_{0.65}\text{MnO}_2$. During this process, the pyrochlore phase fraction grows rapidly and $\text{P2}'\text{-Na}_x\text{MnO}_2$ forms (Figure 1, at $t = 70\text{--}90$ min) before tapering off at the end of the second trajectory in Figure 5 as the amount of $\text{P3-Na}_x\text{MnO}_2$ depletes.

Analysis of the *in situ* diffraction data reveals that selective formation of $\text{Y}_2\text{Mn}_2\text{O}_7$ occurs through two parallel reactions that start during trajectory (ii) in Figure 5:



consistent with the predicted thermodynamic connectivity in Figure 3. In contrast, Li-based assisted metathesis reactions performed at temperatures between 500 °C and 850 °C proceed via LiMnO_2 -based intermediates that result in the direct formation of YMnO_3 phase,^{21,22} which is also predicted from the thermodynamic connectivity (Figure 3a,c).

Based on the stoichiometry of the residual Na-Mn-O phases in each step, there is a loss of $\text{Mn}^{4+} + 2 \text{O}^{2-}$ along with the consumption of Y_2O_3 . Thermodynamically, we expect that stoichiometric NaMnO_2 reacts with Y_2O_3 at a relatively high μ_{O} and low μ_{Mn} (see Figure 3b), as suggested by the average stoichiometry of the transferred species in the parallel cascade of defect reactions (Eqns. 5a and 5b). Curiously, the $\text{Y}_2\text{Mn}_2\text{O}_7$ -forming reaction does not proceed via a typically labile topochemical deintercalation of the alkali cation⁴³ or oxygen anion,^{3,4,44} but instead the chemical potential boundaries shown in Figure 3 guide the reaction to direct formation of the $\text{Y}_2\text{Mn}_2\text{O}_7$ product from the Na-Mn-O intermediates by avoiding the formation of other Y-Mn-O phases.

Conclusions

In assisted metathesis reactions, the presence of an appropriate alkali ion controls the selectivity of the reaction via differences in the thermodynamic stabilities of the reaction intermediates, as defined by the chemical potentials of the constituents in a hyperdimensional compositional space. In the reaction of $3\text{Na}_2\text{CO}_3 + 2\text{YCl}_3 + \text{Mn}_2\text{O}_3$, the $\text{Y}_2\text{Mn}_2\text{O}_7$ pyrochlore forms selectively via the direct reaction of Na_xMnO_2 and Y_2O_3 intermediates, as revealed by *in situ* temperature- and time-dependent SPXRD experiments. However, this pyrochlore selectivity is not achieved with the analogous Li_2CO_3 or K_2CO_3 precursors. Mapping the reaction species in chemical potential space illustrates that NaMnO_2 , and structurally-related compositional variants permit a small difference in local chemical potentials between the $\text{Na}_x\text{Mn}_y\text{O}_2$ intermediates and $\text{Y}_2\text{Mn}_2\text{O}_7$, as the chemical stability windows of structurally homologous $\text{Na}_x\text{Mn}_y\text{O}_2$ phases connect directly with that of $\text{Y}_2\text{Mn}_2\text{O}_7$. The short distance in chemical potential space illustrates why the reaction to form $\text{Y}_2\text{Mn}_2\text{O}_7$ is selective. In contrast, the other alkali-based (Li, K) intermediate phases lack the same degree of structural homology and share different boundaries, thus resulting in the formation of different products. The mechanistic details obtained from crystallographic analysis highlight that the thermodynamic boundaries dictate the reactivity rather than the mobility of an alkali

cation within the oxide framework. This analysis illustrates how local thermodynamic equilibrium principles provide a direct connection to reaction kinetics in guiding the mechanistic pathway of solid-state reactions, thus providing a notion of a protecting group in materials synthesis. The thermodynamic underpinnings permit high-throughput prediction of precursors in higher dimensional chemical spaces that can impart selectivity, kinetic viability, and reversibility.

Supporting Information

- Figures S1-S16: Assisted metathesis reaction energetics, detailed description of the Na-based reaction progression, testing of alternative NaMnO₂ polytypes, *ex situ* control experiments, comparison of neighboring ternary oxide structures in chemical potential space, and Pareto frontier of predicted reactions forming Y₂Mn₂O₇
- Full set of enumerated chemical reactions, experimental raw data, processed data, data processing scripts, and figure plotting scripts

Acknowledgements

This work was supported as part of GENESIS: A Next Generation Synthesis Center, an Energy Frontier Research Center funded by the U.S. Department of Energy, Office of Science, Basic Energy Sciences under Award Number DE-SC0019212. We would also like to acknowledge the facilities at 17-BM-B at the Advanced Photon Source at Argonne National Laboratory and, in particular, the support of A. Yakovenko, W. Wu. JRN acknowledges partial support from a Sloan Research Fellowship.

Theoretical calculations completed in this research used resources of the National Energy Research Scientific Computing Center (NERSC), a U.S. Department of Energy Office of Science User Facility operated under Contract No. DE-AC02-05CH11231.

References

- (1) Stein, A.; Keller, S. W.; Mallouk, T. E. Turning Down the Heat : Design and Mechanism in Solid-State Synthesis. *Science* **1993**, *259*, 1558–1564.
- (2) Murphy, D. W.; Cros, C.; Di Salvo, F. J.; Waszczak, J. V. Preparation and properties of Li_xVS_2 ($0 \leq x \leq 1$). *Inorg. Chem.* **1977**, *16*, 3027–3031.
- (3) Tsujimoto, Y.; Tassel, C.; Hayashi, N.; Watanabe, T.; Kageyama, H.; Yoshimura, K.; Takano, M.; Ceretti, M.; Ritter, C.; Paulus, W. Infinite-layer iron oxide with a square-planar coordination. *Nature* **2007**, *450*, 1062–1065.
- (4) Yajima, T.; Takeiri, F.; Aidzu, K.; Akamatsu, H.; Fujita, K.; Yoshimune, W.; Ohkura, M.; Lei, S.; Gopalan, V.; Tanaka, K.; Brown, C. M.; Green, M. A.; Yamamoto, T.; Kobayashi, Y.; Kageyama, H. A labile hydride strategy for the synthesis of heavily nitridized BaTiO_3 . *Nature Chemistry* **2015**, *7*, 1017–1023.
- (5) Armand, M.; Tarascon, J. M. Building better batteries. *Nature* **2008**, *451*, 652–657.
- (6) Havelia, S.; Wang, S.; Balasubramaniam, K. R.; Schultz, A. M.; Rohrer, G. S.; Salvador, P. A. Combinatorial substrate epitaxy: a new approach to growth of complex metastable compounds. *CrystEngComm* **2013**, *15*, 5434–5441.
- (7) Ding, H.; Dwaraknath, S. S.; Garten, L.; Ndione, P.; Ginley, D.; Persson, K. A. Computational Approach for Epitaxial Polymorph Stabilization through Substrate Selection. *ACS Applied Materials & Interfaces* **2016**, *8*, 13086–13093.
- (8) Miura, A.; Bartel, C. J.; Goto, Y.; Mizuguchi, Y.; Moriyoshi, C.; Kuroiwa, Y.; Wang, Y.; Yaguchi, T.; Shirai, M.; Nagao, M.; Rosero-Navarro, N. C.; Tadanaga, K.; Ceder, G.; Sun, W. Observing and Modeling the Sequential Pairwise Reactions that Drive Solid-State Ceramic Synthesis. *Advanced Materials* **2021**, *33*, 2100312.

- (9) Bianchini, M.; Wang, J.; Clément, R. J.; Ouyang, B.; Xiao, P.; Kitchaev, D.; Shi, T.; Zhang, Y.; Wang, Y.; Kim, H.; Zhang, M.; Bai, J.; Wang, F.; Sun, W.; Ceder, G. The interplay between thermodynamics and kinetics in the solid-state synthesis of layered oxides. *Nat. Mater.* **2020**, *19*, 1088–1095.
- (10) Bonneau, P. R.; Jarvis, R. F.; Kaner, R. B. Rapid solid-state synthesis of materials from molybdenum disulphide to refractories. *Nature* **1991**, *349*, 510–512.
- (11) Wiley, J. B.; Kaner, R. B. Rapid solid-state precursor synthesis of materials. *Science* **1992**, *255*, 1093–1097.
- (12) Miura, A.; Ito, H.; Bartel, C. J.; Sun, W.; Rosero-Navarro, N. C.; Tadanaga, K.; Nakata, H.; Maeda, K.; Ceder, G. Selective metathesis synthesis of MgCr_2S_4 by control of thermodynamic driving forces. *Mater. Horiz.* **2020**, *7*, 1310–1316.
- (13) Wustrow, A.; Key, B.; Phillips, P. J.; Sa, N.; Lipton, A. S.; Klie, R. F.; Vaughey, J. T.; Poepelmeier, K. R. Synthesis and Characterization of MgCr_2S_4 Thiospinel as a Potential Magnesium Cathode. *Inorg. Chem.* **2018**, *57*, 8634–8638.
- (14) Seshadri, R.; Brock, S. L.; Ramirez, A.; Subramanian, M.; Thompson, M. E. Advances in the development and growth of functional materials: Toward the paradigm of materials by design. *MRS Bull.* **2012**, *37*, 682–690.
- (15) Todd, P. K.; Neilson, J. R. Selective Formation of Yttrium Manganese Oxides through Kinetically Competent Assisted Metathesis Reactions. *J. Am. Chem. Soc.* **2019**, *141*, 1191–1195.
- (16) Kamata, K.; Nakajima, T.; Nakamura, T. Thermogravimetric study of rare earth manganites AMnO_3 (A=Sm,Dy,Y,Er,Yb) at 1200°C. *Mater. Res. Bull.* **1979**, *14*, 1007–1012.
- (17) Balakirev, V. F.; Golikov, Y. V. Heterogeneous Phase Equilibria in Rare Earth–Mn–O Systems in Air. *Inorganic Materials* **2003**, *39*, S1–S10.

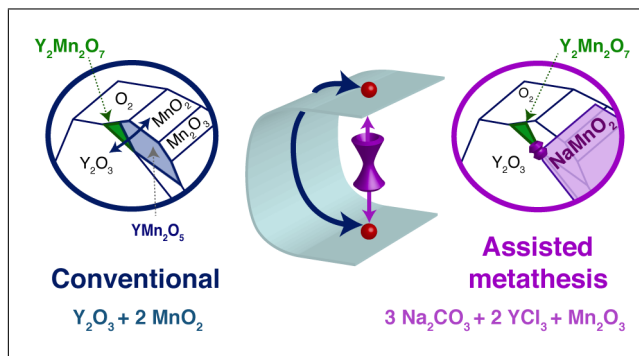
- (18) Fujinaka, H.; Kinomura, N.; Koizumi, M.; Miyamoto, Y.; Kume, S. Syntheses and physical properties of pyrochlore-type $A_2B_2O_7$ ($A = Tl, Y$; $B = Cr, Mn$). *Mater. Res. Bull.* **1979**, *14*, 1133–1137.
- (19) Subramanian, M.; Torardi, C.; Johnson, D.; Pannetier, J.; Sleight, A. Ferromagnetic $R_2Mn_2O_7$ pyrochlores ($R = Dy, Lu, Y$). *J. Solid State Chem.* **1988**, *72*, 24–30.
- (20) Gardner, J. S.; Gingras, M. J. P.; Greedan, J. E. Magnetic pyrochlore oxides. *Rev. Mod. Phys.* **2010**, *82*, 53–107.
- (21) Todd, P. K.; Smith, A. M. M.; Neilson, J. R. Yttrium Manganese Oxide Phase Stability and Selectivity Using Lithium Carbonate Assisted Metathesis Reactions. *Inorg. Chem.* **2019**, *58*, 15166–15174.
- (22) Todd, P. K. et al. Defect-Accommodating Intermediates Yield Selective Low-Temperature Synthesis of $YMnO_3$ Polymorphs. *Inorg. Chem.* **2020**, *59*, 13639–13650.
- (23) Chupas, P. J.; Chapman, K. W.; Kurtz, C.; Hanson, J. C.; Lee, P. L.; Grey, C. P. A versatile sample-environment cell for non-ambient X-ray scattering experiments. *J. Appl. Crystallogr.* **2008**, *41*, 822–824.
- (24) Jiang, Z.; Ramanathan, A.; Shoemaker, D. P. In situ identification of kinetic factors that expedite inorganic crystal formation and discovery. *J. Mater. Chem. C* **2017**, *5*, 5709–5717.
- (25) Yin, L.; Mattei, G. S.; Li, Z.; Zheng, J.; Zhao, W.; Omenya, F.; Fang, C.; Li, W.; Li, J.; Xie, Q.; Zhang, J.-G.; Whittingham, M. S.; Meng, Y. S.; Manthiram, A.; Khalifah, P. G. Extending the limits of powder diffraction analysis: Diffraction parameter space, occupancy defects, and atomic form factors. *Review of Scientific Instruments* **2018**, *89*, 093002.
- (26) Yin, L. et al. Thermodynamics of Antisite Defects in Layered NMC Cathodes: Systematic Insights from High-Precision Powder Diffraction Analyses. *Chem. Mater.* **2020**, *32*, 1002–1010.

- (27) Jain, A.; Ong, S. P.; Hautier, G.; Chen, W.; Richards, W. D.; Dacek, S.; Cholia, S.; Gunter, D.; Skinner, D.; Ceder, G.; Persson, K. A. Commentary: The Materials Project: A materials genome approach to accelerating materials innovation. *APL Mater.* **2013**, *1*, 011002.
- (28) Bartel, C. J.; Millican, S. L.; Deml, A. M.; Rumpitz, J. R.; Tumas, W.; Weimer, A. W.; Lany, S.; Stevanović, V.; Musgrave, C. B.; Holder, A. M. Physical descriptor for the Gibbs energy of inorganic crystalline solids and temperature-dependent materials chemistry. *Nature Communications* **2018**, *9*, 4168.
- (29) Ong, S. P.; Jain, A.; Hautier, G.; Kang, B.; Ceder, G. Thermal stabilities of delithiated olivine MPO_4 (M=Fe, Mn) cathodes investigated using first principles calculations. *Electrochem. Commun.* **2010**, *12*, 427–430.
- (30) Yokokawa, H. Generalized chemical potential diagram and its applications to chemical reactions at interfaces between dissimilar materials. *Journal of Phase Equilibria* **1999**, *20*, 258.
- (31) Patel, A. M.; Nørskov, J. K.; Persson, K. A.; Montoya, J. H. Efficient Pourbaix diagrams of many-element compounds. *Phys. Chem. Chem. Phys.* **2019**, *21*, 25323–25327.
- (32) Virtanen, P. et al. SciPy 1.0: fundamental algorithms for scientific computing in Python. *Nature Methods* **2020**, *17*, 261–272.
- (33) McDermott, M. J.; Dwaraknath, S. S.; Persson, K. A. A graph-based network for predicting chemical reaction pathways in solid-state materials synthesis. *Nature Communications* **2021**, *12*, 3097.
- (34) McDermott, M.; Dwaraknath, S. GENESIS-EFRC/reaction-network: v2.0.3. 2021; <https://doi.org/10.5281/zenodo.5165276>.
- (35) Caballero, A.; Hernán, L.; Morales, J.; Sánchez, L.; Santos Peña, J.; Aranda, M. A. Synthesis and characterization of high-temperature hexagonal $\text{P2-Na}_{0.6}\text{MnO}_2$ and its electrochemical behaviour as cathode in sodium cells. *J. Mater. Chem.* **2002**, *12*, 1142–1147.

- (36) Paulsen, J.; Dahn, J. Studies of the layered manganese bronzes, $\text{Na}_{2/3}[\text{Mn}_{1-x}\text{M}_x]\text{O}_2$ with $\text{M}=\text{Co}, \text{Ni}, \text{Li}$, and $\text{Li}_{2/3}[\text{Mn}_{1-x}\text{M}_x]\text{O}_2$ prepared by ion-exchange. *Solid State Ionics* **1999**, *126*, 3–24.
- (37) Clément, R. J.; Bruce, P. G.; Grey, C. P. Review-Manganese-based P2-type transition metal oxides as sodium-ion battery cathode materials. *J. Electrochem. Soc.* **2015**, *162*, A2589–A2604.
- (38) Jain, A.; Hautier, G.; Ping Ong, S.; Moore, C. J.; Fischer, C. C.; Persson, K. A.; Ceder, G. Formation enthalpies by mixing GGA and GGA + U calculations. *Physical Review B* **2011**, *84*, 45115.
- (39) Martinolich, A. J.; Higgins, R. F.; Shores, M. P.; Neilson, J. R. Lewis Base Mediated Polymorph Selectivity of Pyrite CuSe_2 through Atom Transfer in Solid-State Metathesis. *Chem. Mater.* **2016**, *28*, 1854–1860.
- (40) Schmalzried, H. *Solid state reactions*; Verlag Chemie, 1981.
- (41) Kitchaev, D. A.; Dacek, S. T.; Sun, W.; Ceder, G. Thermodynamics of Phase Selection in MnO_2 Framework Structures through Alkali Intercalation and Hydration. *J. Am. Chem. Soc.* **2017**, *139*, 2672–2681.
- (42) Bai, J.; Sun, W.; Zhao, J.; Wang, D.; Xiao, P.; Ko, J. Y. P.; Huq, A.; Ceder, G.; Wang, F. Kinetic Pathways Templated by Low-Temperature Intermediates during Solid-State Synthesis of Layered Oxides. *Chemistry of Materials* **2020**, *32*, 9906–9913, Publisher: American Chemical Society.
- (43) Neilson, J. R.; McQueen, T. M. Bonding, Ion Mobility, and Rate-Limiting Steps in Deintercalation Reactions with ThCr_2Si_2 -type KNi_2Se_2 . *J. Am. Chem. Soc.* **2012**, *134*, 7750–7757.
- (44) Hayward, M. A.; Green, M. A.; Rosseinsky, M. J.; Sloan, J. Sodium hydride as a powerful

reducing agent for topotactic oxide deintercalation: Synthesis and characterization of the nickel(I) oxide LaNiO_2 . *J. Am. Chem. Soc.* **1999**, *121*, 8843–8854.

Graphical TOC Entry



Supporting Information: Selectivity in yttrium manganese oxide synthesis via local chemical potentials in hyperdimensional phase space

Paul K. Todd,^{†,#} Matthew J. McDermott,^{‡,¶,#} Christopher L. Rom,[†] Adam A. Corrao,[§] Jonathan J. Denney,[§] Shyam S. Dwaraknath,[‡] Peter G. Khalifah,^{§,||}
Kristin A. Persson,^{⊥,¶} and James R. Neilson^{*,†}

[†]*Department of Chemistry, Colorado State University, Fort Collins, Colorado 80523-1872, USA*

[‡]*Materials Sciences Division, Lawrence Berkeley National Laboratory, 1 Cyclotron Road, Berkeley, CA 94720, USA*

[¶]*Department of Materials Science and Engineering, University of California, Berkeley, CA 94720, USA*

[§]*Department of Chemistry, Stony Brook University, Stony Brook, NY 11794-3400, USA*

^{||}*Department of Chemistry, Brookhaven National Laboratory, Upton, NY 11973, USA*

[⊥]*Molecular Foundry, Lawrence Berkeley National Laboratory, 1 Cyclotron Road, Berkeley, CA 94720, USA*

#Contributed equally to this work

E-mail: james.neilson@colostate.edu

Contents

1	Assisted metathesis reaction energetics	S2
2	Detailed description of the Na-based reaction progression	S2
3	Testing of alternative NaMnO₂ polytypes	S8
4	<i>Ex situ</i> control experiments	S10
5	Comparing neighboring ternary oxide structures in chemical potential space	S13
6	Pareto frontier of predicted reactions forming Y₂Mn₂O₇	S14
	References	S21

1 Assisted metathesis reaction energetics

The assisted metathesis net reaction $\text{Mn}_2\text{O}_3 + 2\text{YCl}_3 + 3\text{A}_2\text{CO}_3 + 0.5\text{O}_2 \longrightarrow \text{Y}_2\text{Mn}_2\text{O}_7 + 6\text{A}\text{Cl} + 3\text{CO}_2$ (A= Li, Na, K) is predicted to be exergonic ($G < 0$) for all temperatures (Figure S1). The least negative reaction energy occurs for lithium, followed by sodium, and then potassium.

2 Detailed description of the Na-based reaction progression

Rietveld analysis of the synchrotron X-ray diffraction data presented in Figure 1 provides a quantitative relationship between all crystalline phases that occur at significant phase fractions (> ca. 1%). The first step that is observed along the pathway is formation of yttrium oxychloride and sodium chloride from the reaction between YCl₃ and Na₂CO₃ at 230 °C:



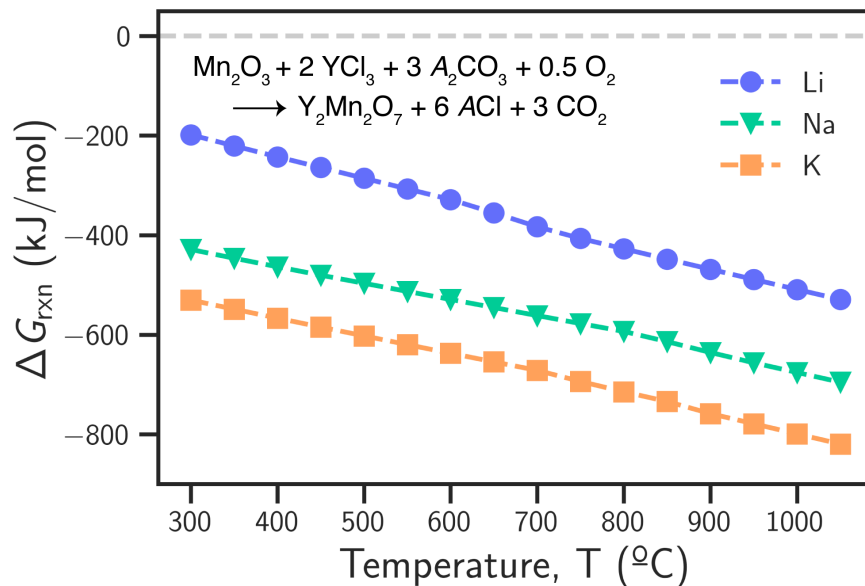


Figure S1: Reaction energetics of the assisted metathesis reaction, $\text{Mn}_2\text{O}_3 + 2 \text{YCl}_3 + 3 \text{A}_2\text{CO}_3 + 0.5 \text{O}_2 \longrightarrow \text{Y}_2\text{Mn}_2\text{O}_7 + 6 \text{ACl} + 3 \text{CO}_2$ for alkali metals $\text{A}=\text{Li}$, Na , and K as predicted by Materials Project data and machine-learned descriptor for solids.¹ Thermochemical data for A_2CO_3 and ACl were acquired from experimental tables²⁻⁴ and CO_2 from the NIST-JANAF database;⁵ hence changes in slope are due to the melting of A_2CO_3 and/or ACl .

The formation of NaCl at 230 °C corresponds directly with the increase in intensity of the $P4/mnm$ YOCl phase and loss of Na_2CO_3 phase intensity, consistent with lithium carbonate assisted metathesis reactions.⁶ YOCl persists over the temperature range 260-490 °C, reacting with more sodium carbonate to form $\text{Y}_3\text{O}_4\text{Cl}$ at 450 °C, and eventually yielding Y_2O_3 at 500 °C. Notably, the particle size of Y_2O_3 remains small (5-40 nm) until its subsequent consumption; the particle microstrain is insignificant in small in all cases (Figure S2).

The precursor Mn_2O_3 remains unreacted until 540 °C when remaining Na_2CO_3 reacts to form the $\text{P3-Na}_x\text{MnO}_2$ intermediate:



consistent with other studies.⁷ The $\text{P3-Na}_x\text{MnO}_2$ intermediate is best described by the monoclinic $C2/m$ P3 layering observed in analogous sodium cobalt oxide structures.^{7,8} As the $\text{P3-Na}_x\text{MnO}_2$ re-

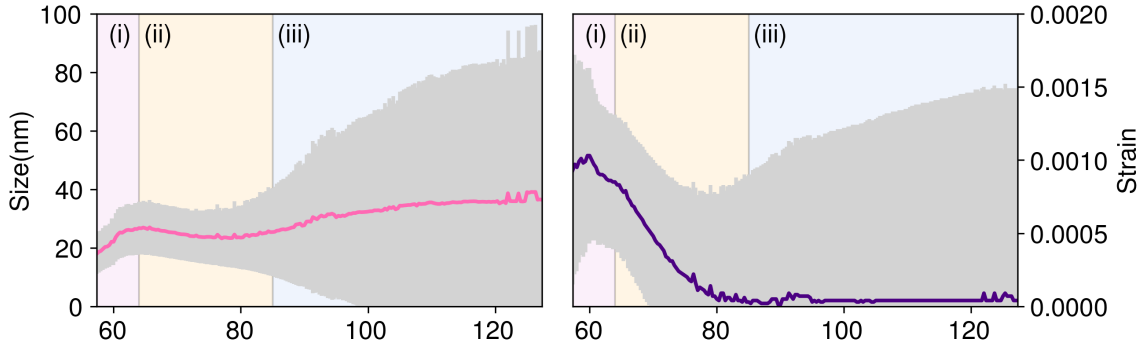
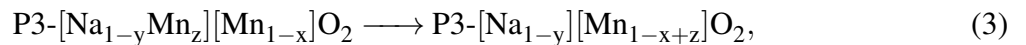


Figure S2: The calculated size and strain values of the coherently diffracting domains of Y_2O_3 intermediates as calculated from the Scherrer equation with error bars using the Integral Breadth method for peak width. The colored regions (i,ii,iii) are taken from Figure 1 and Figure 5.

acts with Y_2O_3 to form the pyrochlore, $P2'-Na_xMnO_2$ also forms. This $P2'-Na_xMnO_2$ intermediate forms in the $Cmcm$ structure where a $P2'$ designation occurs from a slight shift of the MO_2 layers to cause a monoclinic distortion from the idealized $P2-P6_3/mmc$ structure. In $P2'-Na_xMnO_2$, sodium occupies both the prismatic and octahedral sites at fractional occupancy.⁹⁻¹¹

The initial formation of $P3-Na_xMnO_2$ proceeds through a cation-rearrangement reaction where manganese occupying the (8j) sodium site moves to the manganese (2a) site. This is described by following the compositional evolution during the reaction of each crystallographic site on a f^* diagram.¹² To avoid any correlations between atomic displacement parameters and crystallographic site occupancies, we performed many different sequential series of Rietveld refinements with different values for the B_{iso} atomic displacement parameters (Figures S4-S6); the ADP's were held constant to avoid covariances, especially with the multiphased refinement. Using a $B_{iso} = 2 \text{ \AA}^2$ yielded the most reproducible refinements, lowest statistical errors, and small covariances of refined parameters.

To interpret the f^* diagram, trajectory (i) in Figure 5 describes the defect rearrangement reaction:



where the first set of brackets describes the composition of the ideal sodium sites, and the second set of brackets describes that of manganese. The position of the starting composition is calculated as $\text{P3-Na}_{0.35}\text{Mn}_{0.79}\text{O}_2$. At its maximal phase fraction observed in Figure 1, the composition is closer to $\text{Na}_{0.28}\text{Mn}_{0.96}\text{O}_2$. At that point in the overall reaction, this intermediate reacts to form $\text{Y}_2\text{Mn}_2\text{O}_7$.

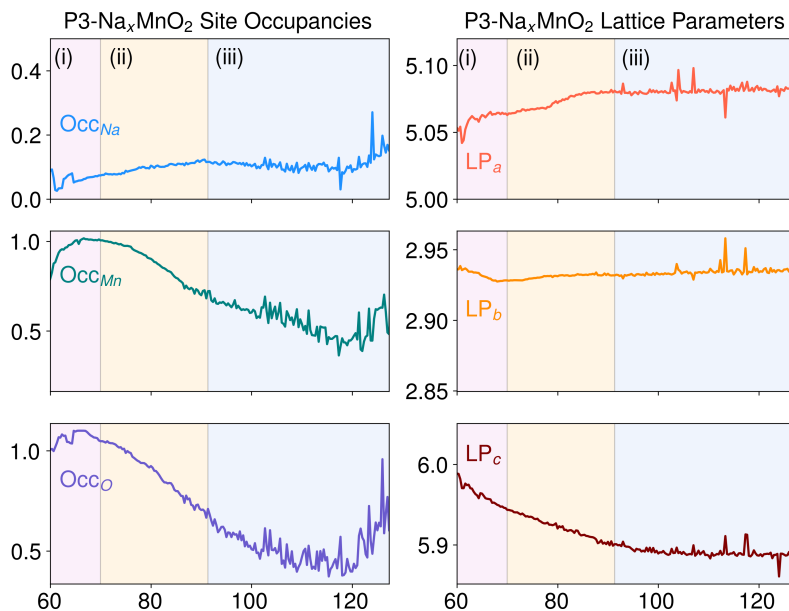
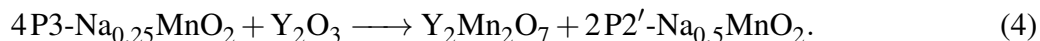


Figure S3: Structural parameters for the $C2/m$ Na_xMnO_2 intermediate as a function of reaction time. Refined occupancies of each atomic site that were used in calculating the f^* ternary diagrams are shown on the right while Unit cell parameters for the monoclinic cell are shown on the left. The colored regions (i,ii,iii) are taken from Figure 1 and Figure 5.

As $\text{Y}_2\text{Mn}_2\text{O}_7$ starts to form (Figure 1), there is a change in the defect chemistry of $\text{P3-Na}_x\text{MnO}_2$. This is indicated by trajectory (ii) in Figure 5 that ends at $\text{Na}_{0.65}\text{MnO}_2$. This result is observed from the decrease in relative electron density from the oxygen site (4i), as well as an increase in the sodium to manganese site ratio. This trend suggests that sodium is either intercalated back into the structure, or that the intermediate loses manganese and oxygen. Figure S3 supports the latter, where the occupancy of both manganese and oxygen decreases as $\text{Y}_2\text{Mn}_2\text{O}_7$ forms, while the interlayer spacing between manganese oxide layers decreases. This provides the

balanced reaction:



During the process described in Eqn. 4, the pyrochlore grows rapidly (Figure 1, 70–90 min) before tapering off at the end of the second trajectory in Figure 5 as the amount of $\text{P3-Na}_x\text{MnO}_2$ depletes.

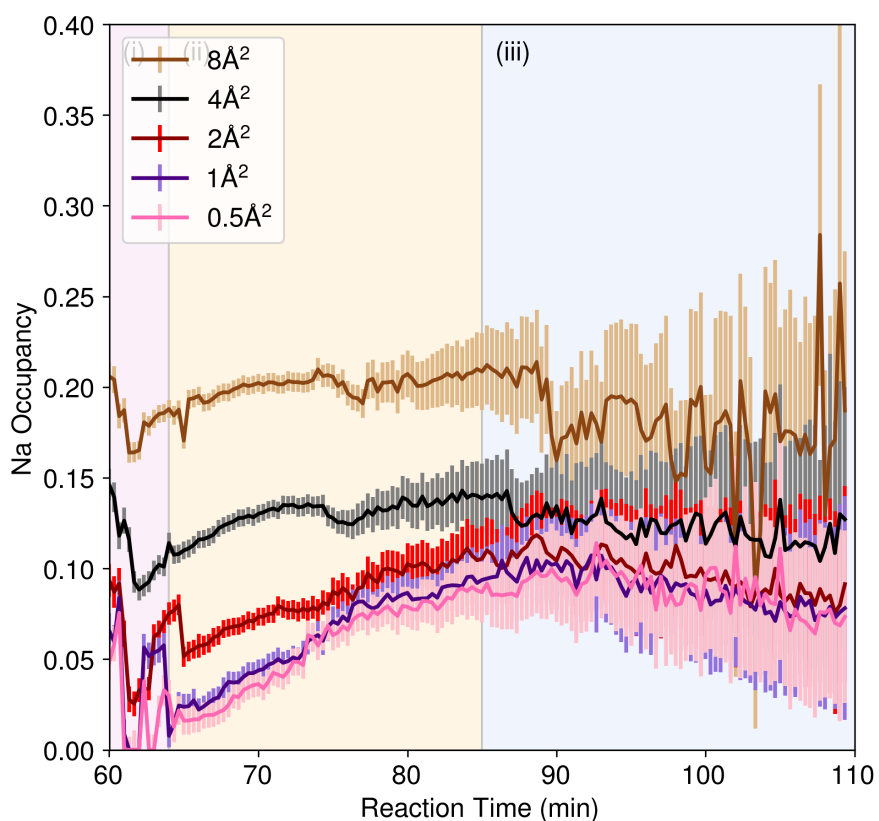


Figure S4: Calculated sodium site occupancy values from sequential Rietveld refinements for the $C2/m$ Na_xMnO_2 intermediate as a function of reaction time at different fixed thermal displacement parameters. The 2 \AA^2 value was used in calculating the f^* ternary diagrams in Figure 5. The colored regions (i,ii,iii) are taken from Figure 1.

Formation of $\text{Y}_2\text{Mn}_2\text{O}_7$ is sustained through the reaction of $\text{P2}'\text{-Na}_x\text{MnO}_2$. Compositional analysis of the $\text{P2}'\text{-Na}_x\text{MnO}_2$ phase on an f^* diagram (Figure S7) reveals that the stoichiome-

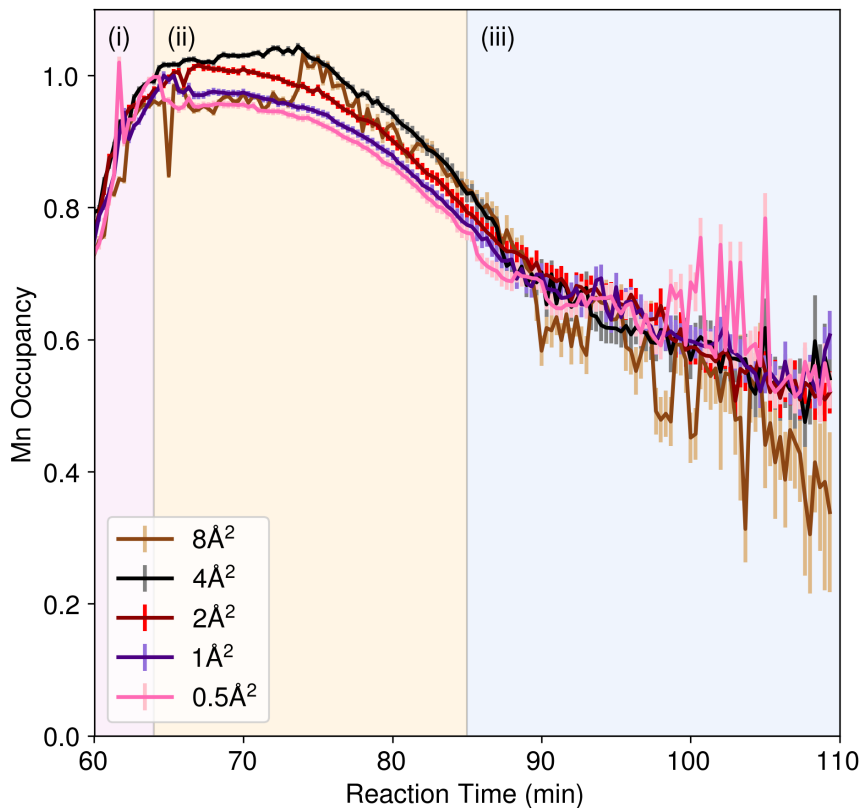
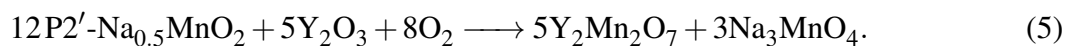


Figure S5: Calculated manganese site occupancy values from sequential Rietveld refinements for the $C2/m$ Na_xMnO_2 intermediate as a function of reaction time at different fixed thermal displacement parameters. The 2 \AA^2 value was used in calculating the f^* ternary diagrams in Figure 5. The colored regions (i,ii,iii) are taken from Figure 1.

try does not deviate systematically away from $\text{Na}_{0.5}\text{MnO}_2$ during the continued course of reaction. Furthermore, the composition of Y_2O_3 does not change during the course of the reaction (Figure S8). The consumption of $\text{P2}'\text{-Na}_{0.5}\text{MnO}_2$ also includes the consumption of Y_2O_3 with production of both $\text{Y}_2\text{Mn}_2\text{O}_7$ and Na_3MnO_4 (Figure 1), as described in the balanced reaction:



This helps to explain the need for excess (flowing) oxygen in the previous study of this reaction.¹³

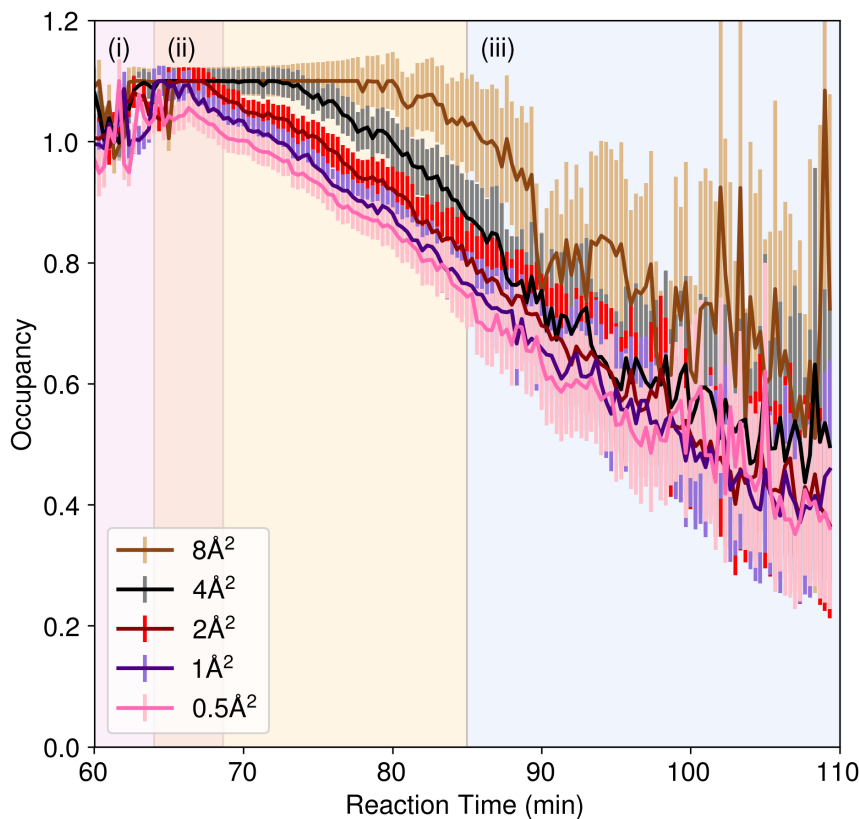


Figure S6: Calculated oxygen site occupancy values from sequential Rietveld refinements for the $C2/m$ Na_xMnO_2 intermediate as a function of reaction time at different fixed thermal displacement parameters. The 2 \AA^2 value was used in calculating the f^* ternary diagrams in Figure 5. The colored regions (i,ii,iii) are taken from Figure 1.

3 Testing of alternative NaMnO_2 polytypes

To determine if the stacking ordering of the manganese-oxygen layers in NaMnO_2 polymorphs affects the observed products, $C2/m$ NaMnO_2 was prepared. This monoclinic polymorph adopts an O3 stacking variant as compared to the $P2'$ $Cmcm$ polymorph. The $C2/m$ polytype differs from the $P2'$ variant by a shift of the layers, and a 60° rotation of all $[\text{MnO}_6]$ octahedra. PXRD results starting with the monoclinic O3 polymorph are presented in Figure S13.

The calculated occupancy of sodium sites in the lattice supports the proposed mechanism to

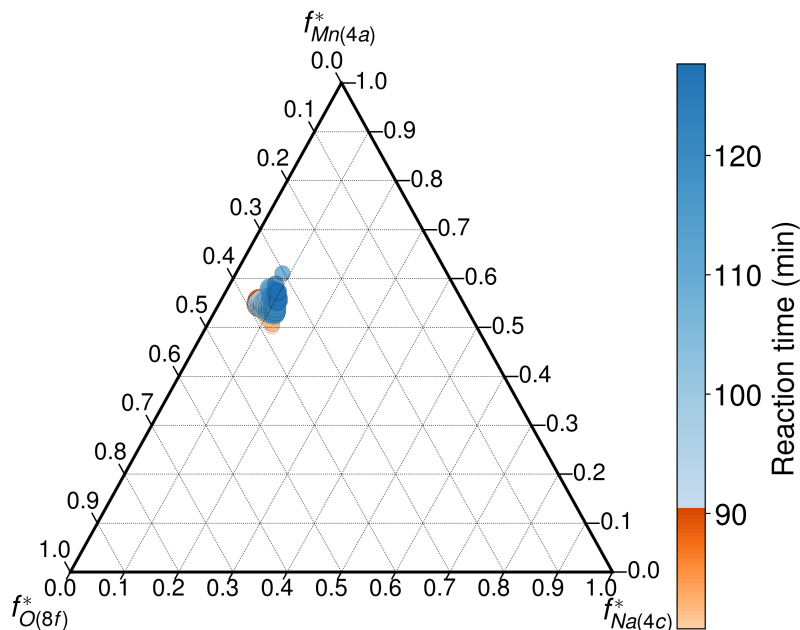


Figure S7: Ternary f^* diagram of atomic coordinates calculated from Rietveld refinement of $Cmc m$ $Na_x MnO_2$. Each axis denotes atom identity and crystallographic Wyckoff position within the lattice. The color bar in the figure is separated into the two defect reactions where the $P2'$ phase is present, as depicted in Figure 1. The diameter of each circle mirrors the calculated Weighted Scale Factor in Figure 1 for $P2'$ - $Na_x MnO_2$.

remove $[MnO_2]$ species. The $Cmc m$ structure has two unique interstitial sodium sites that relate to their position relative to $[MnO_6]$ octahedra. The Na1 site is denoted as the octahedral site, as it sits above and below the $[MnO_6]$ octahedral faces, while the Na2 site shares edges with the $[MnO_6]$ octahedra. The distance between these sodium sites is $\sim 1.6 \text{ \AA}$, thus, both sites cannot be occupied simultaneously, and a fractional occupancy is observed at higher sodium occupancies. The sodium occupancy used in the f^* ternary maps is the summed value of both site occupancies, whereas the individual values are plotted in Figure S9. Interestingly, upon formation of $Na_x MnO_2$ during process (i) (Figure 5, Eqn. 3), only the octahedral Na1 site is occupied, an observation that is supported in $P2$ -type $Na_x MnO_2$ materials with a high degree of cation defects in the structure (e.g., cathode material NMO-420).¹⁴ As these defects are removed during the reaction pathway, the Na2 site populates to reduce electrostatic repulsion. The f^* map suggests that during trajec-

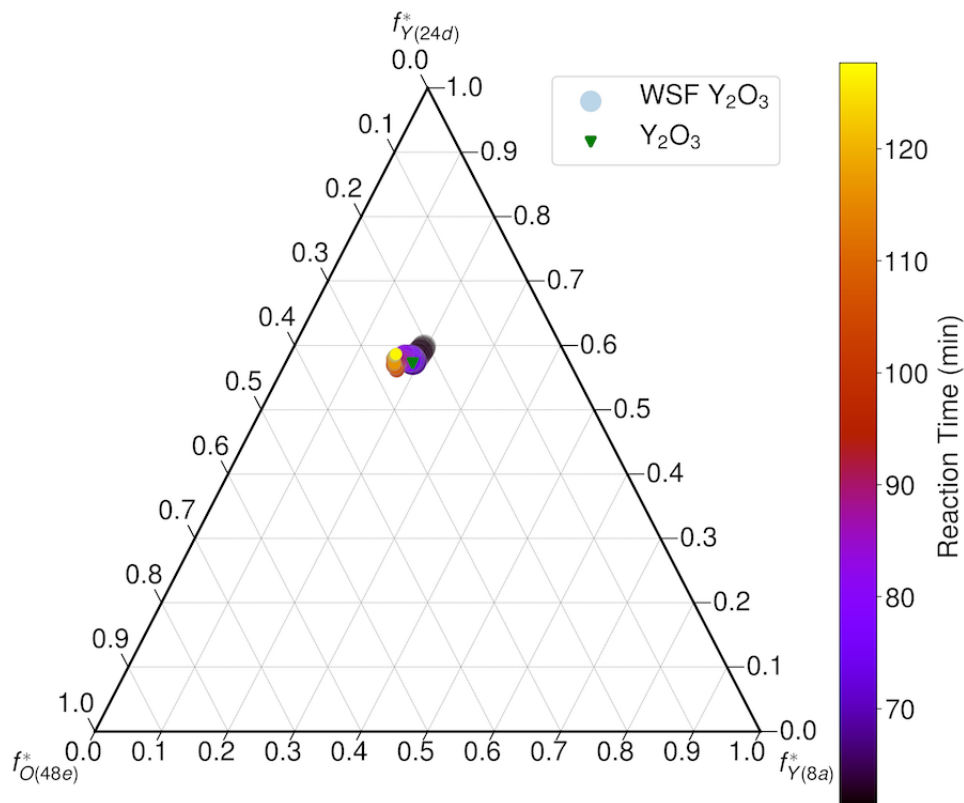


Figure S8: Ternary f^* diagram of atomic coordinates calculated from Rietveld refinement of $Ia\bar{3}$ Y_2O_3 . Each axis denotes atom identity and crystallographic Wyckoff position within the lattice. For reference, the calculated value of Y_2O_3 is provided. The color bar in the figure follows the lifetime of the Y_2O_3 intermediate in the assisted metathesis reaction presented in Figure 1. The diameter of each circle mirrors the calculated Weighted Scale Factor in Figure 1 for Y_2O_3 .

tory (ii), eventually, the occupancy of sodium approaches $NaMnO_2$, which is unusual for P2-type materials where sodium occupancy hits a maximum at 0.7 before a phase transition is observed to O3 type ordering as seen electrochemically.¹¹ This transition is not observed in the diffraction data here suggesting that a higher amount of sodium can be stabilized in the P2 structure at higher temperatures or under non-equilibrium conditions.

4 *Ex situ* control experiments

Control reactions of binary yttrium and manganese oxides reveal that the sodium carbonate assisted metathesis reaction pathway is selective for $Y_2Mn_2O_7$. Analysis of *ex situ* control reactions,

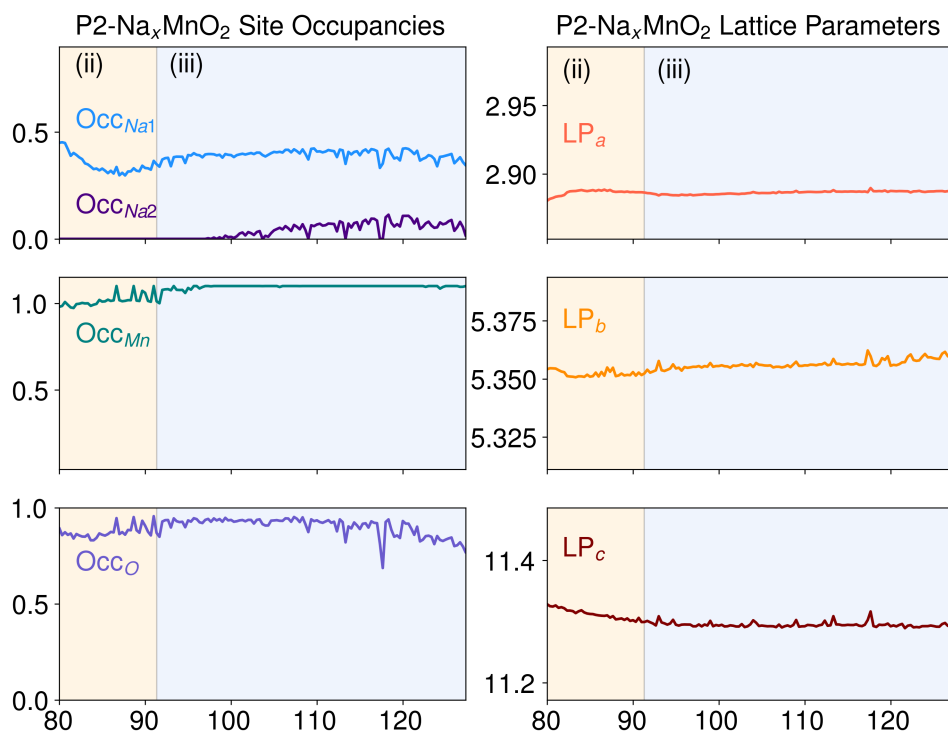


Figure S9: Structural parameters for the $Cmcm$ Na_xMnO_2 intermediate as a function of reaction time. Refined occupancies of each atomic site that were used in calculating the f^* ternary diagrams are shown on the right while Unit cell parameters for the orthorhombic cell are shown on the left. The colored regions (i,ii,iii) are taken from Figure 1 and Figure S7.

$2MnO_2 + Y_2O_3$ and $Mn_2O_3 + Y_2O_3$, performed at $650\text{ }^\circ\text{C}$ under flowing O_2 at ambient pressure (Figure S10) reveal that the reactions contain a finite fraction of $Y_2Mn_2O_7$ at initial time points (i.e., no selectivity), and the phase fraction of $Y_2Mn_2O_7$ decreases at longer times in favor of YMn_2O_5 . Based on Figure 2 this suggests that the true μ_O is near the border between YMn_2O_5 and $Y_2Mn_2O_7$.

Additionally, the presence of a six molar equivalent of sodium chloride does increase the initial yield of $Y_2Mn_2O_7$, but YMn_2O_5 increases in phase fraction at long reaction times (Figure S11). In order to assess the stability of pyrochlore, washed $Y_2Mn_2O_7$ was heated at $650\text{ }^\circ\text{C}$ under flowing oxygen for long-duration reactions. Only partial decomposition occurs to the binary oxides,

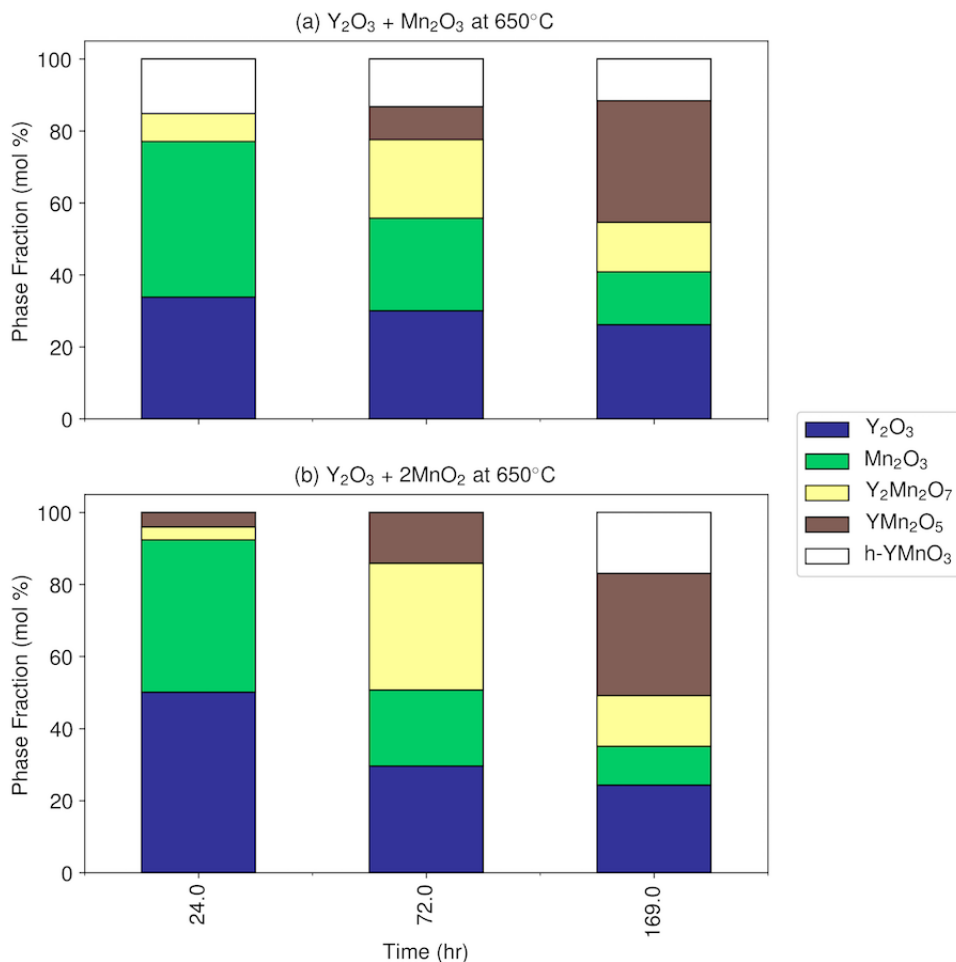


Figure S10: Bar graphs representing the mole percent amounts of products calculated from *ex situ* PXRD Rietveld refinements of the reaction: (a) $\text{Mn}_2\text{O}_3 + \text{Y}_2\text{O}_3 \xrightarrow{\text{O}_2}$ and (b) $2\text{MnO}_2 + \text{Y}_2\text{O}_3 \xrightarrow{\text{O}_2}$. The reactions were heated at $10^\circ\text{C}/\text{min}$ to 650°C for 24, 72, and 128 hours under flowing oxygen. Each color bar is represented in the legend as a different product phase.

$\text{Mn}_2\text{O}_3 + \text{Y}_2\text{O}_3$, after 24 h; the composition remains constant even after heating for 2 weeks (Figure S12).

Control ternary metathesis reactions performed using nominally stoichiometric, ideal sodium manganese oxide precursors do not yield selectivity for $\text{Y}_2\text{Mn}_2\text{O}_7$. In the case of Li_2CO_3 -based assisted metathesis reactions,¹³ we previously identified that the ternary metathesis reaction, $\text{LiMnO}_2 + \text{YOCl} \longrightarrow \text{YMnO}_3 + \text{LiCl}$ yielded improved selectivity for orthorhombic YMnO_3 over the analogous assisted metathesis reactions.⁶ However, the reaction, $2\text{NaMnO}_2 + 2\text{YOCl} \xrightarrow{\text{O}_2}$, results in a mixture of Y-Mn-O products (Figure S13). Furthermore, using a partially-oxidized precursor in

the reaction, $\text{P2-2Na}_{0.7}\text{MnO}_2$ with 2 YOCl selectively yields $\text{Y}_2\text{Mn}_2\text{O}_7$, but it is incomplete after 24 h (Figure S14). Together, these control reactions lend support to the sodium-based reaction pathway in selectively yielding $\text{Y}_2\text{Mn}_2\text{O}_7$.

5 Comparing neighboring ternary oxide structures in chemical potential space

Comparing the accessibility and similarity of ternary oxide structures offers insight into why the assisted metathesis reaction proceeds differently across the different alkali species. The structures of the possible stoichiometric A-Mn-O ternary oxide intermediates are illustrated in Figure S15. The sodium-based phases (Figure S15a) show a strong preference for the layered Birnessite, $\delta\text{-MnO}_2$, framework. As illustrated by the gray shaded areas in Figure 3b, the compositions of neighbors to NaMnO_2 (mp-18957) that move towards higher μ_{O} include NaMn_2O_4 (mp-1002571), NaMn_4O_8 (mp-1016155) and $\text{Na}_2\text{Mn}_3\text{O}_7$ (mp-19080). Note that the $\text{Na}_2\text{Mn}_3\text{O}_7$ phase has a layered crystal structure akin to NaMnO_2 , but with regularly ordered Mn vacancies; this phase is experimentally observed in trace quantities in 24 h reactions at 650 °C.¹³ For values of $x \leq 0.25$ in Na_xMnO_2 (e.g., NaMn_4O_8), the Hollandite $\alpha\text{-MnO}_2$ framework was previously shown to be thermodynamically favorable;¹⁵ however, the layered NaMn_4O_8 (mp-1016155) phase is predicted to be stable at $T = 650$ °C.

In contrast, in the Li-Mn-O system (Figure S15b), as one looks at phases towards higher μ_{O} starting from the layered LiMnO_2 (mp-754656), all neighboring phases would require a structural rearrangement (and thus kinetic barrier) as they become deficient in lithium. Nearly all of the subsequent phases prefer a spinel-like connectivity, which consists of three-dimensionally interconnected layers of edge-connected manganese-oxygen octahedra, including LiMn_2O_4 (mp-1097867, pictured), $\text{Li}_4\text{Mn}_5\text{O}_{12}$ (mp-691115), and $\text{Li}_{11}\text{Mn}_{13}\text{O}_{32}$ (mp-531021). A closer look at LiMn_2O_4 reveals that a polymorph with a layered structure is predicted (mp-1176656); however, it is 0.046 eV/atom above the hull (at $T = 650$ °C).

Finally, in the K-Mn-O system (Figure S15c), the predicted ground state KMnO_2 (mp-554900) phase is not of a layered MnO_2 framework; although, the layered phase (mp-1002570) is about 0.044 eV/atom above the hull at $T = 650$ °C. In the K-deficient regime, the layered phase dominates, but KMn_2O_4 (mp-1003314) is predicted to be metastable (0.007 eV/atom above hull). The layered structures KMn_3O_6 (mp-1016190) and KMn_4O_8 (mp-1003312) are both predicted to be stable, however. As in the Li-Mn-O system, accessing these K-deficient phases from the ground-state stoichiometric KMnO_2 phase would require structural rearrangement, posing a significant kinetic barrier. Experimentally, K_2CO_3 -based assisted metathesis reactions do yield some $\text{Y}_2\text{Mn}_2\text{O}_7$ product at 650 °C; however, the reaction is not selective for $\text{Y}_2\text{Mn}_2\text{O}_7$,¹³ which is consistent with this analysis.

6 Pareto frontier of predicted reactions forming $\text{Y}_2\text{Mn}_2\text{O}_7$

As was demonstrated in a recent work on predicting solid-state synthesis routes,¹⁶ a candidate set of several recommended reactions can be generated by calculating the Pareto frontier along the reaction distribution shown in Figure 4. This is shown in Figure S16, and the corresponding reactions are shown in Table S1. In particular, the reaction $\text{O}_2 + 4 \text{Y}_3\text{BrO}_4 + 4 \text{KMn}_3\text{O}_6 \longrightarrow 4 \text{KBr} + 6 \text{Y}_2\text{Mn}_2\text{O}_7$ stands out as a promising alternative reaction with a zero total chemical potential distance and moderately negative reaction energy. However, it requires KMn_3O_6 as a precursor, which to our knowledge, has not been previously experimentally synthesized.

Table S1: Predicted reactions which lie on the Pareto frontier in $\Delta\Phi_{\text{rxn}}$ and $\sum\Delta\mu_{\text{min}}$

Reaction	$\Delta\Phi_{\text{rxn}}$ (eV/at.)	$\sum\Delta\mu_{\text{min}}$ (eV/at.)
$4 \text{YCl}_3 + 4 \text{Na}_3\text{MnO}_4 \longrightarrow \text{O}_2 + 12 \text{NaCl} + 2 \text{Y}_2\text{Mn}_2\text{O}_7$	-0.444	0.219
$\text{O}_2 + 4 \text{YOCl} + 4 \text{NaMnO}_2 \longrightarrow 4 \text{NaCl} + 2 \text{Y}_2\text{Mn}_2\text{O}_7$	-0.303	0.055
$\text{O}_2 + \text{YMnO}_3 + 0.5 \text{RbI} \longrightarrow 0.5 \text{Y}_2\text{Mn}_2\text{O}_7 + 0.5 \text{RbIO}_3$	-0.258	0.035
$\text{O}_2 + 4 \text{Y}_3\text{BrO}_4 + 4 \text{KMn}_3\text{O}_6 \longrightarrow 4 \text{KBr} + 6 \text{Y}_2\text{Mn}_2\text{O}_7$	-0.159	0.000
$3.667 \text{K}_2\text{MnO}_4 + 0.5 \text{Y}_2\text{O}_3 \longrightarrow \text{O}_2 + 0.667 \text{K}_{11}\text{Mn}_4\text{O}_{16} + 0.5 \text{Y}_2\text{Mn}_2\text{O}_7$	0.016	0.000
$0.2667 \text{Y}(\text{IO}_3)_3 + 0.2667 \text{MnO}_2 \longrightarrow \text{O}_2 + 0.1333 \text{Y}_2\text{Mn}_2\text{O}_7 + 0.8 \text{I}$	0.439	0.409

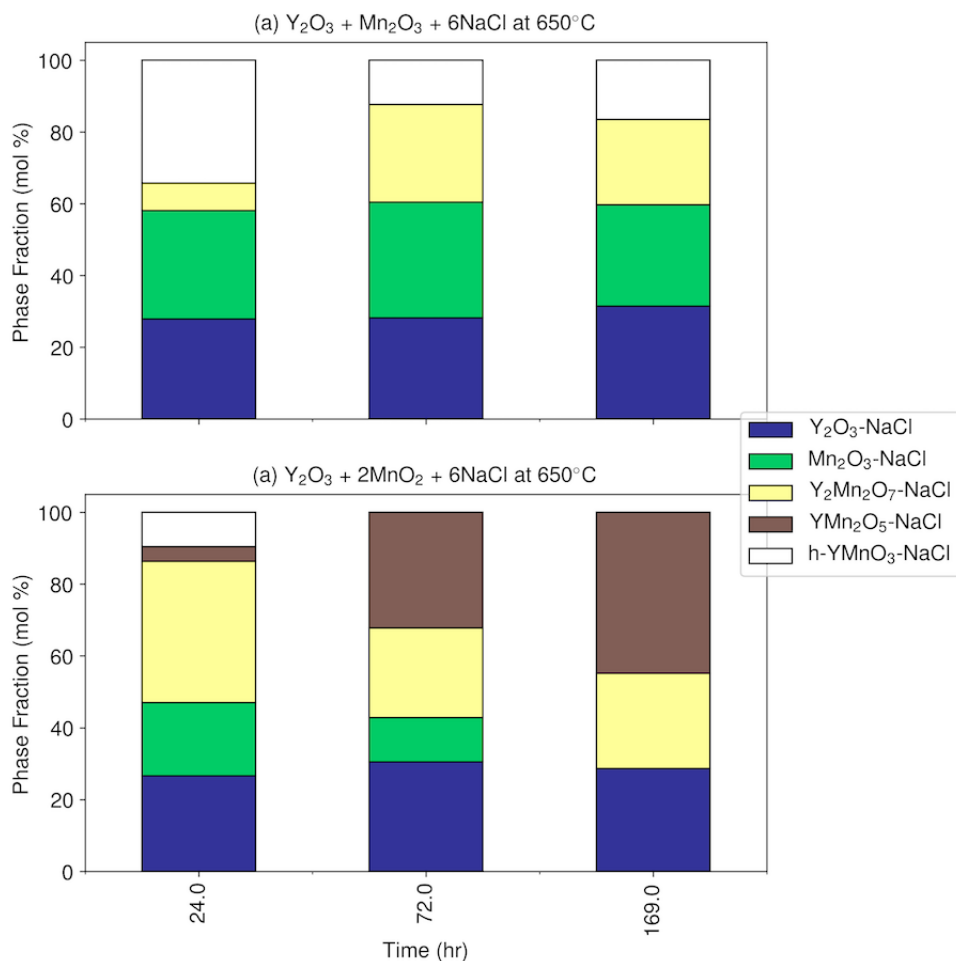


Figure S11: Bar graphs representing the mole percent amounts of products calculated from *ex situ* PXRD Rietveld refinements of the reaction: (a) $Mn_2O_3 + Y_2O_3 \xrightarrow{6NaCl, O_2}$ and (b) $2MnO_2 + Y_2O_3 \xrightarrow{6NaCl, O_2}$. The reactions were heated at $10^\circ C/min$ to $650^\circ C$ for 24, 72, and 128 hours under flowing oxygen. Each color bar is represented in the legend as a different product phase. Mole fractions are presented after subtracting the contribution from NaCl for comparison.

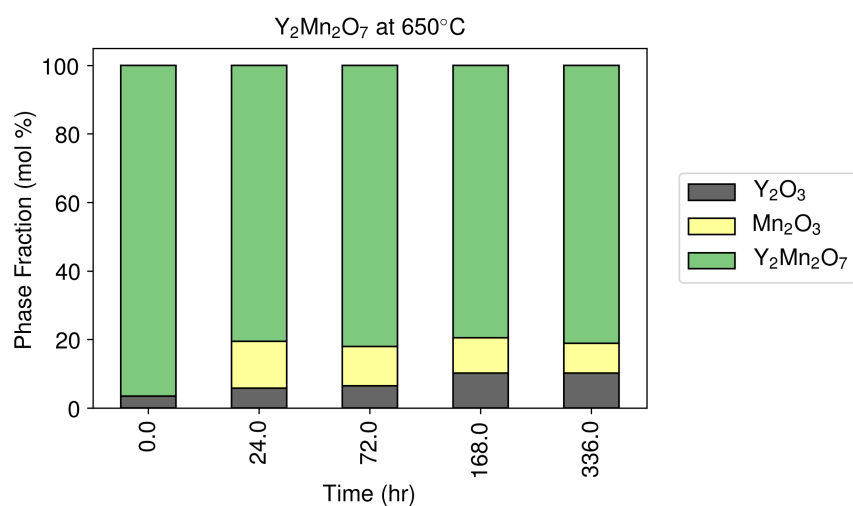


Figure S12: Bar graphs representing the mole percent amounts of products calculated from *ex situ* PXRD Rietveld refinements of $Y_2Mn_2O_7$. The reactions were heated at 10 °C/min to 650 °C for 24, 72, 128, and 336 hours under flowing oxygen. Each color bar is represented in the legend as a different calculated phase.

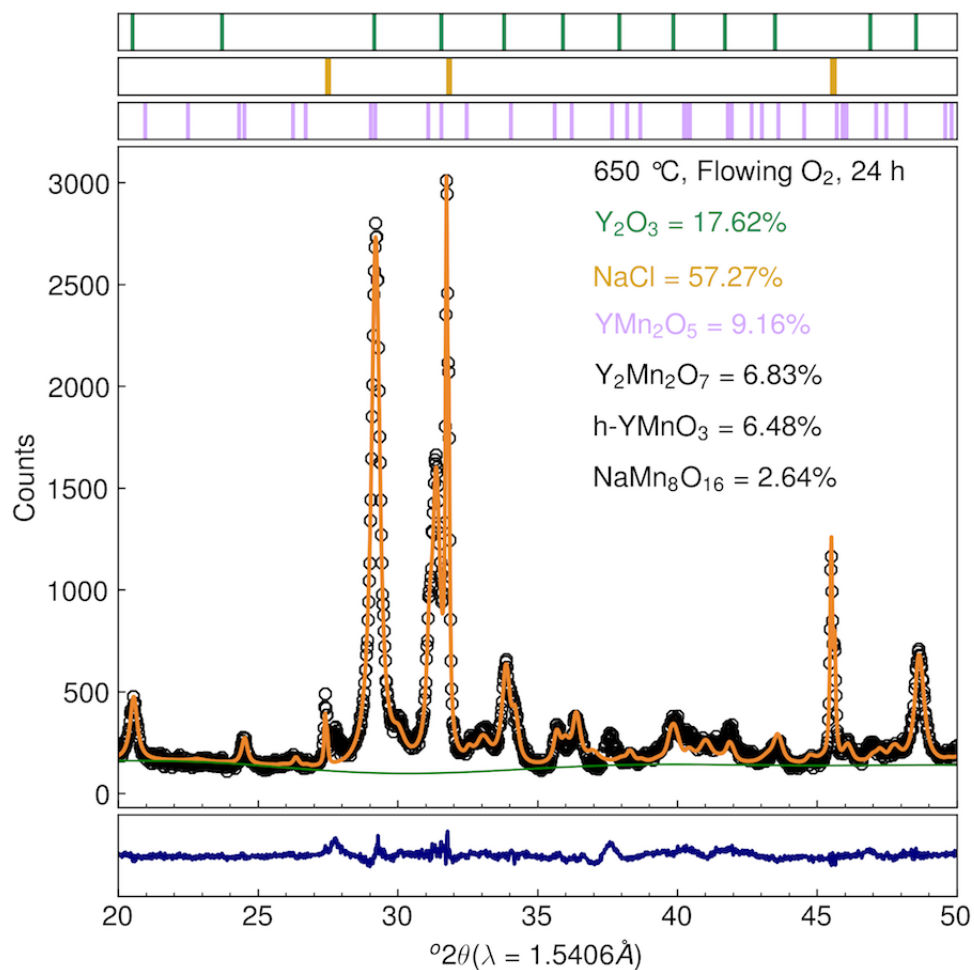


Figure S13: PXRD results from the reaction: $C2/m \text{ NaMnO}_2 + \text{YOCl} \xrightarrow{\text{O}_2}$. The reaction was performed by heating at 10 °C/min to 650 °C and dwelling for 24 h. Raw data: black circles, Rietveld refinement: orange, background: green, difference: navy. Tick marks denote the majority phases and are highlighted by color and mole percent as calculated from Rietveld refinements. All other product mole percents are highlighted in black without tick marks.

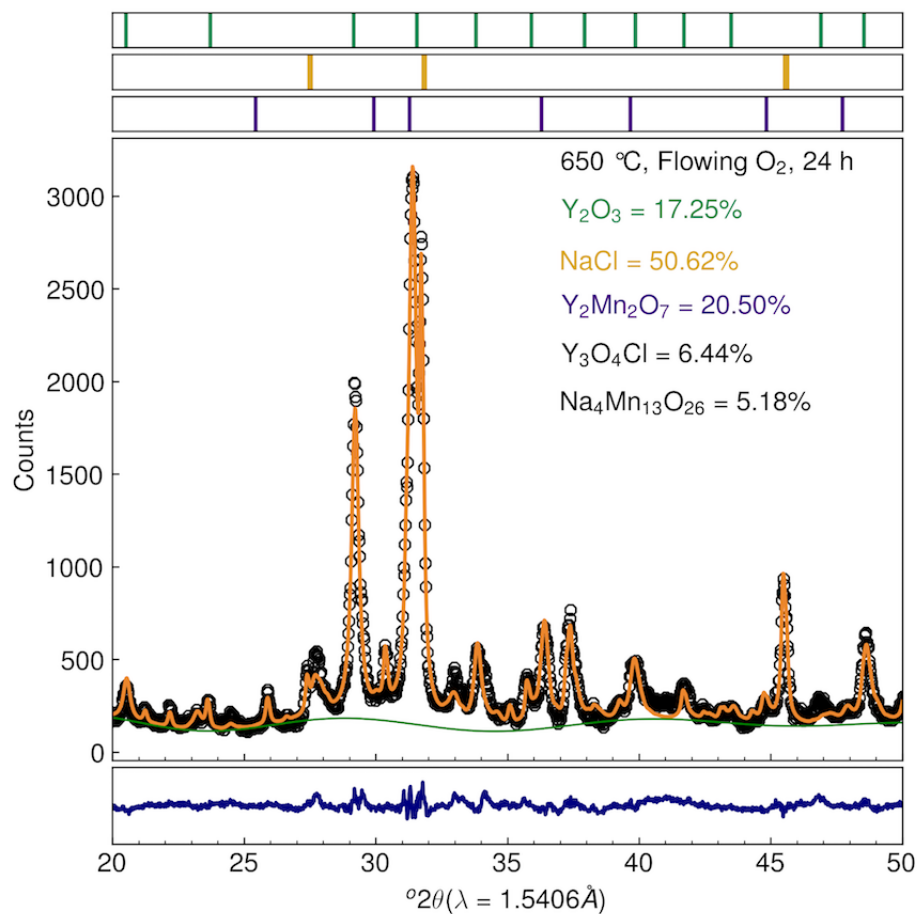
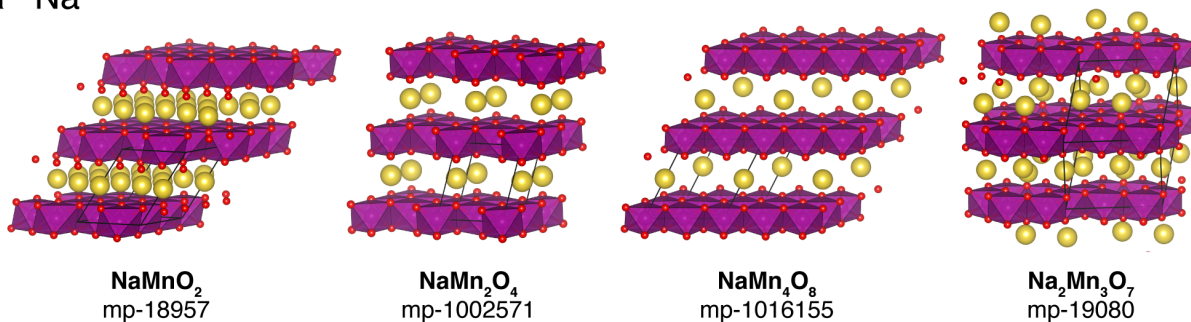
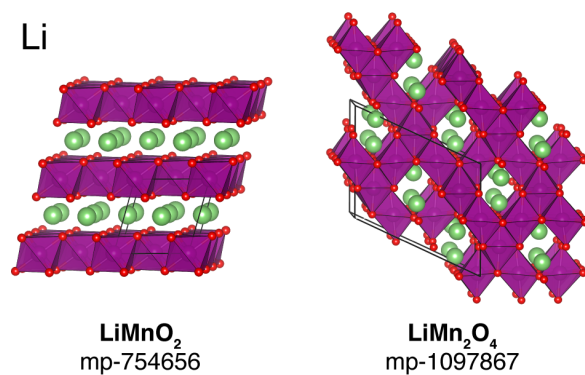


Figure S14: PXRD results from the reaction: $Cmcm \text{ Na}_{0.7}\text{MnO}_2 + \text{YOCl} \xrightarrow{\text{O}_2}$. The reaction was performed by heating at 10 °C/min to 650 °C and dwelling for 24 h. Raw data: black circles, Rietveld refinement: orange, background: green, difference: navy. Tick marks denote the majority phases and are highlighted by color and mole percent as calculated from Rietveld refinements. All other product mole percents are highlighted in black without tick marks.

a Na



b Li



c K

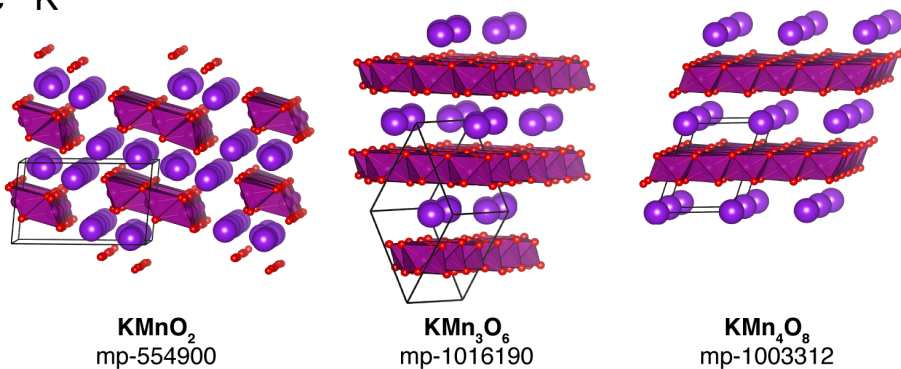


Figure S15: Structures of possible stoichiometric A-Mn-O ternary oxide intermediates predicted to be stable at $T = 650$ °C for A equal to **a**, Na, **b**, Li, **c**, K. Unit cells are drawn and each structure's Materials Project ID (mp-id) is provided.

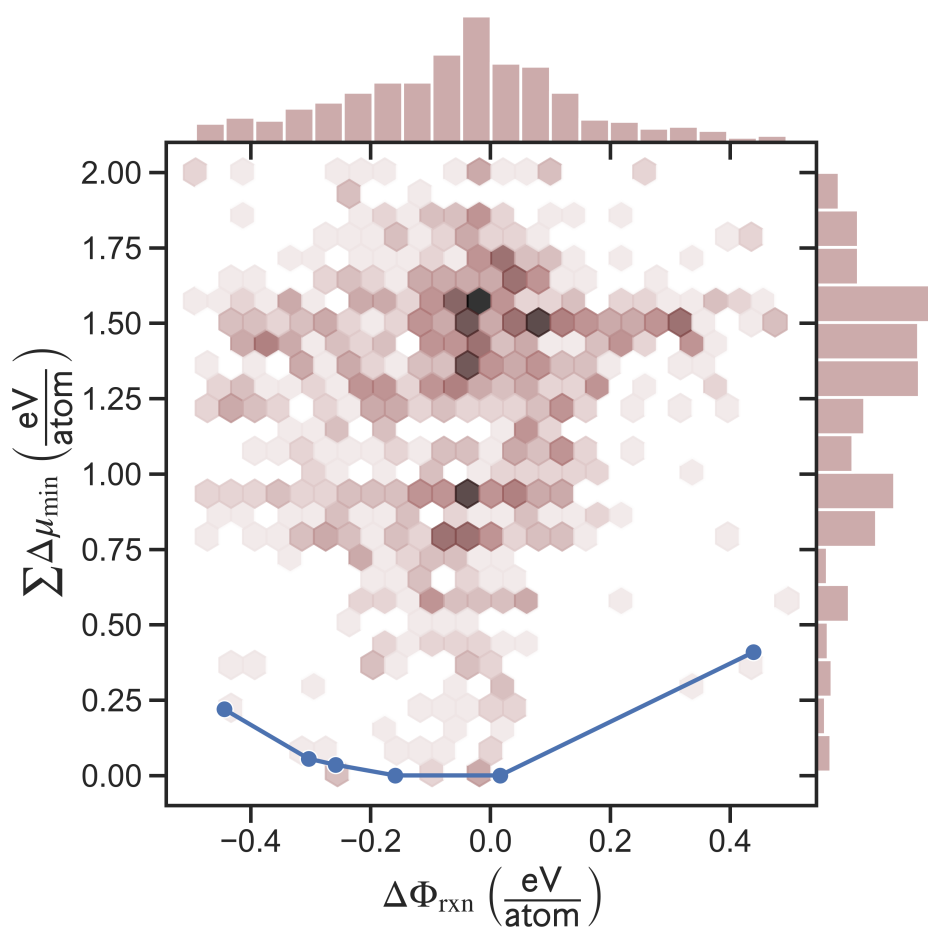


Figure S16: Energy and total chemical potential distance distribution for 3,017 predicted chemical reactions forming $\text{Y}_2\text{Mn}_2\text{O}_7$. The Pareto frontier is given by the blue line. Reactions along this frontier, shown as blue dots, are reproduced in Table S1.

References

- (1) Bartel, C. J.; Millican, S. L.; Deml, A. M.; Rumpitz, J. R.; Tumas, W.; Weimer, A. W.; Lany, S.; Stevanović, V.; Musgrave, C. B.; Holder, A. M. Physical descriptor for the Gibbs energy of inorganic crystalline solids and temperature-dependent materials chemistry. *Nature Communications* **2018**, *9*, 4168.
- (2) Barin, I. *Thermochemical Data of Pure Substances*; John Wiley and Sons, Ltd, 2008; Chapter 12, pp 925–992.
- (3) Barin, I. *Thermochemical Data of Pure Substances*; John Wiley and Sons, Ltd, 2008; Chapter 12, pp 1080–1237.
- (4) Barin, I. *Thermochemical Data of Pure Substances*; John Wiley and Sons, Ltd, 2008; Chapter 12, pp 844–924.
- (5) Malcolm W. Chase, J. *NIST-JANAF thermochemical tables*; Fourth edition. Washington, DC: American Chemical Society; New York: American Institute of Physics for the National Institute of Standards and Technology, 1998.
- (6) Todd, P. K.; Smith, A. M. M.; Neilson, J. R. Yttrium Manganese Oxide Phase Stability and Selectivity Using Lithium Carbonate Assisted Metathesis Reactions. *Inorg. Chem.* **2019**, *58*, 15166–15174.
- (7) Bianchini, M.; Wang, J.; Clément, R. J.; Ouyang, B.; Xiao, P.; Kitchaev, D.; Shi, T.; Zhang, Y.; Wang, Y.; Kim, H.; Zhang, M.; Bai, J.; Wang, F.; Sun, W.; Ceder, G. The interplay between thermodynamics and kinetics in the solid-state synthesis of layered oxides. *Nat. Mater.* **2020**, *19*, 1088–1095.
- (8) Takada, K.; Osada, M.; Izumi, F.; Sakurai, H.; Takayama-Muromachi, E.; Sasaki, T. Characterization of Sodium Cobalt Oxides Related to P3-Phase Superconductor. *Chemistry of Materials* **2005**, *17*, 2034–2040.

- (9) Caballero, A.; Hernán, L.; Morales, J.; Sánchez, L.; Santos Peña, J.; Aranda, M. A. Synthesis and characterization of high-temperature hexagonal P2-Na_{0.6}MnO₂ and its electrochemical behaviour as cathode in sodium cells. *J. Mater. Chem.* **2002**, *12*, 1142–1147.
- (10) Paulsen, J.; Dahn, J. Studies of the layered manganese bronzes, Na_{2/3}[Mn_{1-x}M_x]O₂ with M=Co, Ni, Li, and Li_{2/3}[Mn_{1-x}M_x]O₂ prepared by ion-exchange. *Solid State Ionics* **1999**, *126*, 3–24.
- (11) Clément, R. J.; Bruce, P. G.; Grey, C. P. Review-Manganese-based P2-type transition metal oxides as sodium-ion battery cathode materials. *J. Electrochem. Soc.* **2015**, *162*, A2589–A2604.
- (12) Yin, L.; Mattei, G. S.; Li, Z.; Zheng, J.; Zhao, W.; Omenya, F.; Fang, C.; Li, W.; Li, J.; Xie, Q.; Zhang, J.-G.; Whittingham, M. S.; Meng, Y. S.; Manthiram, A.; Khalifah, P. G. Extending the limits of powder diffraction analysis: Diffraction parameter space, occupancy defects, and atomic form factors. *Review of Scientific Instruments* **2018**, *89*, 093002.
- (13) Todd, P. K.; Neilson, J. R. Selective Formation of Yttrium Manganese Oxides through Kinetically Competent Assisted Metathesis Reactions. *J. Am. Chem. Soc.* **2019**, *141*, 1191–1195.
- (14) Stoyanova, R.; Carlier, D.; Sendova-Vassileva, M.; Yoncheva, M.; Zhecheva, E.; Nih-tianova, D.; Delmas, C. Stabilization of over-stoichiometric Mn⁴⁺ in layered Na_{2/3}MnO₂. *J. Solid State Chem.* **2010**, *183*, 1372–1379.
- (15) Kitchaev, D. A.; Dacek, S. T.; Sun, W.; Ceder, G. Thermodynamics of Phase Selection in MnO₂ Framework Structures through Alkali Intercalation and Hydration. *J. Am. Chem. Soc.* **2017**, *139*, 2672–2681.
- (16) Aykol, M.; Montoya, J. H.; Hummelshøj, J. Rational Solid-State Synthesis Routes for Inorganic Materials. *Journal of the American Chemical Society* **2021**, *143*, 9244–9259, Publisher: American Chemical Society.